Underwater Acoustic Communication Using Multiple-Input Multiple-Output Doppler-Resilient Orthogonal Signal Division Multiplexing

Tadashi Ebihara, *Member, IEEE,* Hanako Ogasawara and Geert Leus, *Fellow, IEEE*

Abstract

In this paper, we propose a novel underwater acoustic communication scheme that achieves energy and spectrum efficiency simultaneously by combining Doppler-resilient orthogonal signal division multiplexing (D-OSDM) and multiple-input multiple-output (MIMO) signaling. We present both the transmitter and receiver processing for MIMO D-OSDM. We evaluate the performance of MIMO D-OSDM in simulations with a large inter-symbol interference of 25 symbols and a Doppler spread with a maximum Doppler shift of 8 Hz. In addition, the sea trial is performed in Suruga Bay, where the receiver is mounted on a barge and a research vessel with the transmitter makes round-trips along a line with a speed of 4 kt. In the experiments, we obtain an inter-symbol interference of 3.6 – 29.7 symbols and a Doppler spread of several Hertz (leading to a spread over 2–3 subcarrier spacings). The simulation results suggest that MIMO D-OSDM has an advantage over normal D-OSDM, Doppler-resilient MIMO orthogonal frequency division multiplexing (MIMO D-OFDM) and classical OFDM with MIMO signaling (MIMO OFDM) – MIMO D-OSDM achieves better bit-error-rate performance than the benchmarks. The sea trial results also support the advantage of MIMO D-OSDM – MIMO D-OSDM achieves a coded block error rate of 3.2% while normal D-OSDM and MIMO D-OFDM achieve a coded block error rate of 9.7 and 9.3%, respectively. We conclude that MIMO D-OSDM can become a viable technique that achieves reliable and effective UWA communication.

Index Terms

Underwater (UWA) communication, delay spread, Doppler spread

I. Introduction

Recently, underwater wireless communication systems have diversified dramatically. Multiple media (e.g., acoustic [1], [2], optical [3], and radio [4]) have been utilized to satisfy system requirements such as communication range and speed. Among these systems, underwater acoustic (UWA) communication offers a wide area connectivity, since acoustic waves propagate over long distances in the underwater environment.

Although UWA communication has the potential to provide wide-area connectivity, achieving reliable and high-speed UWA communication is still challenging. This is because UWA communication suffers from the large delay and Doppler spreads of the UWA channel, whose impact is much larger than for land mobile RF communication [5]. To achieve reliable communication in such doubly spread channels, numerous physical layer technologies using single-carrier [6], [7], [8], [9] and multi-carrier [e.g., orthogonal frequency division multiplexing (OFDM)] [10], [11], [12], [13], [14], [15], [16], [17] approaches have been proposed. In addition, the combination of advanced hardware and signal processing techniques, such as multiple-input multiple-output (MIMO) signaling, have also been considered to improve the effective data rate [18], [19], [20], [21], [22].

To achieve reliable UWA communication, we have proposed Doppler-resilient orthogonal signal division multiplexing (hereafter, we call this normal D-OSDM) [23], [24]. Normal D-OSDM is a communication technique for a single user and it is a combination of OSDM [25] and orthogonal multiple access [26]; it places the pilot and data signals on a rectangular lattice in the time-frequency domain so that they do not interfere even in doubly spread channels. This signal structure enables the receiver to counteract the delay-Doppler spread of the UWA channel efficiently, resulting in a reduction of the required transmission power. We have tested normal D-OSDM in simulations and test-tank experiments and have found that normal D-OSDM can reduce the power consumption requirements compared to the latest techniques based on orthogonal frequency division multiplexing (OFDM). In addition, we have also conducted a demonstration of normal D-OSDM in a harbor with a mobile receiver and confirmed that normal D-OSDM delivers excellent reliability in an actual UWA environment [27]. However, normal D-OSDM has a small spectrum efficiency, a limitation that should be addressed before we utilize this technique in an actual underwater application.

In this paper, we combine single-user multiple-input multiple-output (MIMO) signaling and normal D-OSDM to achieve both energy- and spectrum-efficient UWA communication. There exist several advanced MIMO techniques in underwater acoustic communication to enhance the communication quality, such as space-time, space-frequency, space-time-frequency MIMO [20], [28], [29]. Furthermore, the study of multi-user MIMO systems, where multiple transmitters transmit multiple data streams to their corresponding receiver using MIMO, has emerged recently as an important topic to establish an UWA network [21]. However, the scope of this paper is to maximize the transmission rate of a single user, since high data rate transmission systems providing a significant robustness against delay and Doppler spread are of great importance for UWA communication. Hence, we only consider a traditional MIMO system for a single-user environment in this paper. Furthermore, traditional single-user

MIMO OFDM is the most popular form of UWA communication using MIMO [18], [19], [22]. Considering all the above, we prefer to combine traditional single-user MIMO signaling (with different data streams on different antennas) with OSDM, and we employ normal D-OSDM and the well-known OFDM techniques [Doppler-resilient MIMO OFDM (MIMO D-OFDM) and classical MIMO OFDM] as benchmarks [18].

We develop the transmitter and receiver processing for MIMO D-OSDM and show that MIMO D-OSDM can improve the spectrum efficiency while preserving the characteristics of D-OSDM in terms of its resilience against delay and Doppler spreads. We also evaluate the performance of MIMO D-OSDM in doubly spread channels in both simulations and sea trials.

Section II explains the signal processing flow of MIMO D-OSDM at the transmitter and receiver. Section III evaluates its performance in simulations. Section IV evaluates its performance in sea trials. Section V concludes this work.

Notation: We use upper/lower bold face letters to denote matrices/row vectors. We define $x[i]$ as the i-th element of the vector $\boldsymbol{x}$ starting with index 0. We use upper/lower bold face letters to denote matrices/row vectors. $(\cdot)^*$, $(\cdot)^{\mathrm{T}}$, and $(\cdot)^{-1}$ denote conjugate transpose, transpose, and inverse, respectively. The set of nonnegative integer numbers and positive integer numbers are defined as $\mathbb{Z}^*$ and $\mathbb{Z}^+$, respectively. $\mathbf{0}_{R\times C}$, $\boldsymbol{F}_N$, and $\boldsymbol{I}_M$ represent the $R\times C$ all-zero matrix, the $N\times N$ inverse discrete Fourier transform (IDFT) matrix and the $M\times M$ identity matrix, respectively. W_{MN} represents the basic element of the IDFT matrix, i.e., $W_{MN} = \exp\left[2\pi\sqrt{-1}/(MN)\right]/\sqrt{MN}$. $\boldsymbol{Z}_M$ is a cyclic shift matrix of size $M\times M$, i.e.,

$$\boldsymbol{Z}_M = \begin{pmatrix} 0 & 1 & 0 & \cdots & 0 \\ 0 & 0 & 1 & \cdots & 0 \\ \vdots & \vdots & \vdots & \ddots & 0 \\ 0 & 0 & 0 & \cdots & 1 \\ 1 & 0 & 0 & \cdots & 0 \end{pmatrix}.$$

II. MIMO D-OSDM

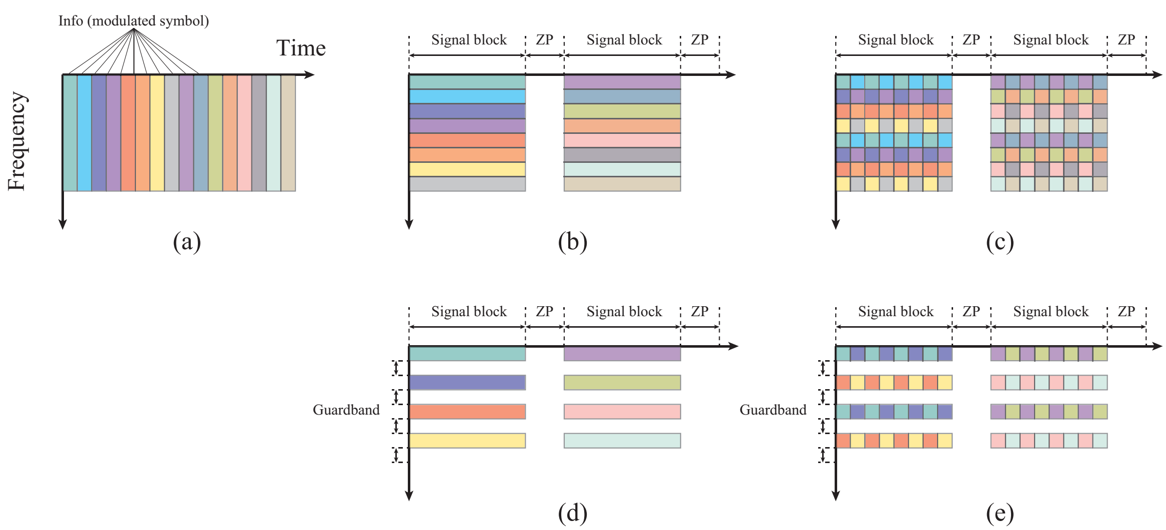

Fig. 1. Time-frequency structure of communication signals: (a) single-carrier, (b) OFDM, (c) OSDM, (d) D-OFDM and (e) D-OSDM.

A. Overview of OSDM and D-OSDM

Before describing MIMO D-OSDM, we would like to overview the basics of our OSDM and D-OSDM technology. Figure 1 shows the time-frequency structure of baseband communication signals that are considered for UWA communication, where each colored box represents the information (modulated symbol). In the well-known single-carrier system, the information appears once in the time domain [Fig. 1(a)]. In an OFDM system, the information is transmitted block-by-block [with a zero-padded (ZP) suffix to avoid interblock interference] and each information appears once in the frequency domain [Fig. 1(b)]. On the other hand, in OSDM, the modulated symbols periodically appear in both the time and frequency domain [Fig. 1(c)]. In our previous work, we found that such signal structure gives resilience against large delay spreads, and that OSDM outperforms single-carrier and OFDM systems in a test tank for a static environment [25]. However, we also found that the performance of OSDM drops in a dynamic environment, since the symbols interfere in the frequency domain (intercarrier interference; ICI) due to Doppler spread.

To cope with the Doppler spread in UWA channels, the use of carefully spaced null subcarriers was found to be effective in OFDM systems (D-OFDM) [11]. In D-OFDM, null subcarriers are inserted between subcarriers (where each modulated symbol is allocated in each subcarrier) to prevent adjacent-carrier interference [Fig. 1(d)]. To give Doppler-resilience as in D-OFDM, we proposed D-OSDM, by combining OSDM and orthogonal multiple access [26]. In D-OSDM, null subcarriers are inserted between subcarriers as in D-OFDM [Fig. 1(e)]. Furthermore, we found that D-OSDM is robust to both large delay and Doppler spreads, and D-OSDM outperforms D-OFDM (D-OSDM requires a lower signal transmission power to achieve the same error probability as D-OFDM) in a test tank for a dynamic environment, in exchange for effective data rate (spectrum efficiency) and receiver complexity [24].

In the following subsections, we would like to combine single-user MIMO signaling and D-OSDM to achieve both energy- and spectrum-efficient UWA communication.

B. Signal Processing at the Transmitter

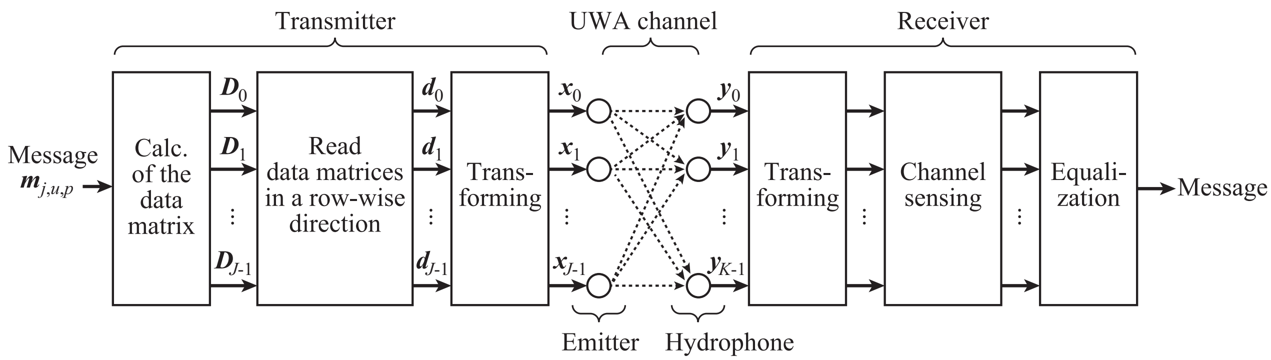

Fig. 2. Signal processing flow of MIMO D-OSDM at the transmitter and receiver.

TABLE I
Parameters used for the design of MIMO D-OSDM

Message vector length	$M \in \mathbb{Z}^+$
Total number of message vectors per message block	$P \in \mathbb{Z}^+$
Total number of message blocks	$U \in \mathbb{Z}^+$
Maximum Doppler shift	$Q \in \mathbb{Z}^*$
Total number of pilot vector, message vectors, and zero vectors in a data matrix	$N = 1 + 2Q + U(P + 2Q)$
Delay spread length of the UWA channel	$L \in \mathbb{Z}^+$ $(L \leq M)$
Measurable delay spread in MIMO system	$\tilde{L} = \lfloor L/J \rfloor$
Number of emitters at Tx	$J \in \mathbb{Z}^+$
Number of hydrophones at Rx	$K \in \mathbb{Z}^+$ $(J \leq K)$

We would like to show the signal processing flow of MIMO D-OSDM at the transmitter (Tx) and receiver (Rx) employing J emitters and K hydrophones, respectively (Fig. 2), using parameters and notations shown in Tables I and II, respectively. The Tx calculates the transmission signal $\boldsymbol{x}_j$ $(j = 0, 1, \ldots, J-1)$ from message data vectors $\boldsymbol{m}_{j,u,p}$ $(u = 0, 1, \ldots, U-1$ and $p = 0, 1, \ldots, P-1)$, whose elements are complex modulated symbols. The signal processing steps at the Tx can be described as follows:

(i) Create data matrices $\boldsymbol{D}_j$ as

$$\begin{aligned}\boldsymbol{D}_j = \Big(\boldsymbol{p}_j^{\mathrm{T}}, \boldsymbol{0}_{2Q\times M}^{\mathrm{T}},\quad & \boldsymbol{m}_{j,0,0}^{\mathrm{T}}, \boldsymbol{m}_{j,0,1}^{\mathrm{T}}, \ldots, \boldsymbol{m}_{j,0,P-1}^{\mathrm{T}}, \boldsymbol{0}_{2Q\times M}^{\mathrm{T}},\\ & \boldsymbol{m}_{j,1,0}^{\mathrm{T}}, \boldsymbol{m}_{j,1,1}^{\mathrm{T}}, \ldots, \boldsymbol{m}_{j,1,P-1}^{\mathrm{T}}, \boldsymbol{0}_{2Q\times M}^{\mathrm{T}}, \ldots\\ & \ldots \boldsymbol{m}_{j,U-1,0}^{\mathrm{T}}, \boldsymbol{m}_{j,U-1,1}^{\mathrm{T}}, \ldots, \boldsymbol{m}_{j,U-1,P-1}^{\mathrm{T}}, \boldsymbol{0}_{2Q\times M}^{\mathrm{T}}, \Big)^{\mathrm{T}},\end{aligned} \tag{1}$$

where the structure of $\boldsymbol{D}_j$ is shown in Fig. 3. Q corresponds to the maximum (discrete) Doppler shift of the UWA channel. $\boldsymbol{p}_j$ is a pilot vector and it is shared between the Tx and Rx prior to the communication. More specifically, based on one common pilot vector $\boldsymbol{p}$ the pilot vector $\boldsymbol{p}_j$ is constructed as

$$\boldsymbol{p}_j = \boldsymbol{p}(\boldsymbol{Z}_M)^{j\tilde{L}}, \tag{2}$$

$$\tilde{L} = \lfloor L/J \rfloor. \tag{3}$$

Here, L corresponds to a rough estimate of the delay spread length of the UWA channel. The reason for constructing the different pilot vectors this way will become clear later on.

TABLE II
NOTATIONS USED FOR THE DESIGN OF MIMO D-OSDM (E:EMITTER AND H:HYDROPHONE)

Name	Size	Notation
Common pilot vector	$1 \times M$	$\boldsymbol{p}$
Pilot vector from E#j	$1 \times M$	$\boldsymbol{p}_j$
Message vector	$1 \times M$	$\boldsymbol{m}_{j,u,p}$
Combination of $\boldsymbol{m}_{j,u,p}$ for all p	$1 \times MP$	$\boldsymbol{m}_{j,u}$
Data matrix	$N \times M$	$\boldsymbol{D}_j$
Data vector by reading $\boldsymbol{D}_j$ in a row-wise direction	$1 \times MN$	$\boldsymbol{d}^{\mathrm{r}}_j$
Transmit signal block from E#j	$1 \times MN$	$\boldsymbol{x}_j$
Channel impulse response (E#j →H#k, Doppler shift of q)	$1 \times MN$	$\boldsymbol{h}^{j\to k}_q$
Channel matrix via a basis expansion model using $\boldsymbol{h}^{j\to k}_q$	$MN \times MN$	$\boldsymbol{H}^{j\to k}_q$
Diagonal matrix to represent Doppler shift of q	$MN \times MN$	$\boldsymbol{\Lambda}_q$
Received signal at hydrophone #k	$1 \times MN$	$\boldsymbol{y}_k$
Additive noise on $\boldsymbol{y}_k$	$1 \times MN$	$\boldsymbol{n}_k$
Delay-Doppler channel matrix	$MN \times MN$	$\boldsymbol{C}^{j\to k}$
– Submatrix of $\boldsymbol{C}^{j\to k}$	$M \times M$	$\boldsymbol{C}^{j\to k}_{n,q}$
– Approximated $\boldsymbol{C}^{j\to k}_{n,q}$	$M \times M$	$\tilde{\boldsymbol{C}}^{j\to k}_{n,q}$
Combined $\boldsymbol{C}^{j\to k}$ for all j and k	$JMN \times KMN$	$\boldsymbol{C}_{\mathrm{a}}$
Transformed received signal (combined $\boldsymbol{y}_k$ for all k)	$1 \times KMN$	$\boldsymbol{z}$
– Subvector of $\boldsymbol{z}$	$1 \times MN$	$\boldsymbol{z}_k$
—- Additive noise on $\boldsymbol{z}_k$	$1 \times MN$	$\boldsymbol{\eta}_k$
—- Left-side part of $\boldsymbol{z}_k$	$1 \times M(Q+1)$	$\boldsymbol{z}^{0\to Q}_{\mathrm{p},k}$
—- Middle part of $\boldsymbol{z}_k$	$1 \times M(P+2Q)$	$\boldsymbol{z}_{k,u}$
—- Right-side part of $\boldsymbol{z}_k$	$1 \times MQ$	$\boldsymbol{z}^{-Q\to -1}_{\mathrm{p},k}$
—— Element of $\boldsymbol{z}^{0\to Q}_{\mathrm{p},k}$	$1 \times M(Q+1)$	$\boldsymbol{z}^{0\to Q}_{\mathrm{p},j,k}$
—— Element of $\boldsymbol{z}^{-Q\to -1}_{\mathrm{p},k}$	$1 \times MQ$	$\boldsymbol{z}^{-Q\to -1}_{\mathrm{p},j,k}$
—— Element of $\boldsymbol{z}_{k,u}$	$1 \times M(P+2Q)$	$\boldsymbol{z}_{j,k,u}$
—— Noise component on $\left(\boldsymbol{z}^{-Q\to -1}_{\mathrm{p},k}, \boldsymbol{z}^{0\to Q}_{\mathrm{p},k}\right)$	$1 \times M(1+2Q)$	$\boldsymbol{\eta}_{\mathrm{p},k}$
—— Additive noise on $\boldsymbol{z}_{k,u}$	$1 \times M(P+2Q)$	$\boldsymbol{\eta}_{k,u}$
Approximated channel matrix obtained from pilot	$M \times M$	$\tilde{\boldsymbol{C}}^{k}_{0,q}$
Approximated and combined channel matrix to obtain message	$JMP \times KM(P+2Q)$	$\boldsymbol{C}_{\mathrm{cu}}$
– Submatrix of $\boldsymbol{C}_{\mathrm{cu}}$	$MP \times M(P+2Q)$	$\boldsymbol{C}^{j\to k}_{\mathrm{cu}}$
Noise component on received message	$1 \times MP$	$\tilde{\boldsymbol{\eta}}_{j,u}$

(ii) Convert data matrices $\boldsymbol{D}_j$ to vectors $\boldsymbol{d}^{\mathrm{r}}_j$ by reading $\boldsymbol{D}_j$ in a *row*-wise direction as

$$\boldsymbol{d}^{\mathrm{r}}_j = (\boldsymbol{p}_j, \boldsymbol{0}_{1\times 2QM}, \boldsymbol{m}_{j,0}, \boldsymbol{0}_{1\times 2QM}, \boldsymbol{m}_{j,1}, \boldsymbol{0}_{1\times 2QM}, \ldots, \ldots, \boldsymbol{m}_{j,U-1}, \boldsymbol{0}_{1\times 2QM}). \tag{4}$$

where

$$\boldsymbol{m}_{j,u} = (\boldsymbol{m}_{j,u,0}, \boldsymbol{m}_{j,u,1}, \ldots, \boldsymbol{m}_{j,u,P-1}). \tag{5}$$

(iii) Calculate the transmit signal block $\boldsymbol{x}_j$ by applying a transformation matrix to $\boldsymbol{d}^{\mathrm{r}}_j$ as

$$\boldsymbol{x}_j = \boldsymbol{d}^{\mathrm{r}}_j (\boldsymbol{F}_N \otimes \boldsymbol{I}_M), \tag{6}$$

where '⊗' is the Kronecker product. By this transformation, the pilot and data blocks appear on a rectangular lattice in the time-frequency domain so that they do not interfere even in doubly spread channels.

(iv) Add L zeros to the signal block $\boldsymbol{x}_j$ (zero-padding) and emit $\boldsymbol{x}_j$ from emitter #j. The transmission happens simultaneous for all emitters resulting in a boost of the effective data rate.

Note that the above signal processing flow of MIMO D-OSDM is the same as that of D-OSDM [24] when $J = 1$. Furthermore, classical MIMO OFDM and MIMO D-OFDM can be calculated by reading the data matrices $\boldsymbol{D}_j$ in a *column*-wise direction and applying an inverse fast Fourier transform when $J = 1$ and $J > 1$, respectively. In that case, the transmit signal block of size $1 \times MN$ becomes

$$\boldsymbol{x}^{\mathrm{OFDM}}_j = \boldsymbol{d}^{\mathrm{c}}_j \boldsymbol{F}_{MN}, \tag{7}$$

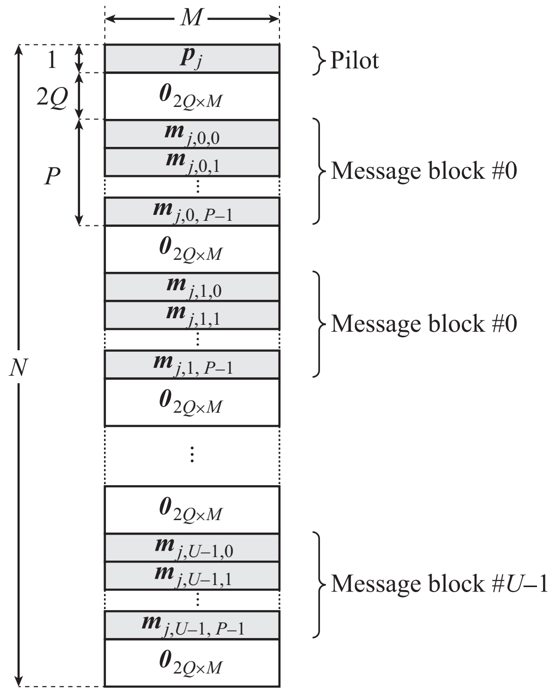

Fig. 3. Structure of data matrix $\boldsymbol{D}_j$.

where $\boldsymbol{d}_j^{\mathrm{c}}$ is a vector of size $1 \times MN$ that is obtained by reading $\boldsymbol{D}_j$ in a *column*-wise direction.

$$\begin{aligned}
\boldsymbol{d}_j^{\mathrm{c}} \quad = (p_j[0], \mathbf{0}_{1\times 2Q}, \quad & m_{j,0,0}[0], m_{j,0,1}[0], \ldots, m_{j,0,P-1}[0], \mathbf{0}_{1\times 2Q}, \\
& m_{j,1,0}[0], m_{j,1,1}[0], \ldots, m_{j,1,P-1}[0], \mathbf{0}_{1\times 2Q}, \ldots \\
& \ldots, m_{j,U-1,0}[0], m_{j,U-1,1}[0], \ldots, m_{j,U-1,P-1}[0], \mathbf{0}_{1\times 2Q}, \\
p_j[1], \mathbf{0}_{1\times 2Q}, \quad & m_{j,0,0}[1], m_{j,0,1}[1], \ldots, m_{j,0,P-1}[1], \mathbf{0}_{1\times 2Q}, \\
& m_{j,1,0}[1], m_{j,1,1}[1], \ldots, m_{j,1,P-1}[1], \mathbf{0}_{1\times 2Q}, \ldots \\
& \ldots, m_{j,U-1,0}[1], m_{j,U-1,1}[1], \ldots, m_{j,U-1,P-1}[1], \mathbf{0}_{1\times 2Q}, \ldots \\
\ldots, p_j[M-1], \mathbf{0}_{1\times 2Q}, \quad & m_{j,0,0}[M-1], m_{j,0,1}[M-1], \ldots, m_{j,0,P-1}[M-1], \mathbf{0}_{1\times 2Q}, \\
& m_{j,1,0}[M-1], m_{j,1,1}[M-1], \ldots, m_{j,1,P-1}[M-1], \mathbf{0}_{1\times 2Q}, \ldots \\
& \ldots, m_{j,U-1,0}[M-1], m_{j,U-1,1}[M-1], \ldots, m_{j,U-1,P-1}[M-1], \mathbf{0}_{1\times 2Q}).
\end{aligned} \tag{8}$$

C. Signal Processing at the Receiver

In the UWA channel, the transmitted signal blocks $\boldsymbol{x}_j$ interfere with each other. In addition, $\boldsymbol{x}_j$ is affected by delay and Doppler spreads, and is received by the Rx with K hydrophones. The Rx receives K signals simultaneously and obtains sequences $\boldsymbol{y}_k$ ($k = 0, 1, \ldots, K-1$), by an overlap-add operation on each received signal. The obtained sequence can be expressed using a basis expansion model (BEM) [30] as follows:

$$\boldsymbol{y}_k = \sum_{j=0}^{J-1} \left\{ \boldsymbol{x}_j \sum_{q=-Q}^{Q} \left(\boldsymbol{H}_q^{j\to k} \boldsymbol{\Lambda}_q \right) \right\} + \boldsymbol{n}_k, \tag{9}$$

where $\boldsymbol{n}_k$ represents the additive noise component. $\boldsymbol{H}_q^{j\to k}$ and $\boldsymbol{\Lambda}_q$ represent the effect of the delay and Doppler spreads, respectively,

$$\boldsymbol{H}_q^{j\to k} = \begin{pmatrix} h_q^{j\to k}[0] & h_q^{j\to k}[1] & \cdots & h_q^{j\to k}[MN-1] \\ h_q^{j\to k}[MN-1] & h_q^{j\to k}[0] & \cdots & h_q^{j\to k}[MN-2] \\ \vdots & \vdots & \ddots & \vdots \\ h_q^{j\to k}[1] & h_q^{j\to k}[2] & \cdots & h_q^{j\to k}[0] \end{pmatrix}, \tag{10}$$

$$\boldsymbol{\Lambda}_q = \mathrm{diag}\left[W_{MN}^{0}, W_{MN}^{q}, \ldots, W_{MN}^{(MN-1)q} \right]. \tag{11}$$

Here, $h_q^{j\to k}[m]$ ($h_q^{j\to k}[m] = 0$ when $m > L$) is the channel impulse response from emitter #j to hydrophone #k at Doppler scale q.

The relationship between $\boldsymbol{d}_j^{\mathrm{r}}$ and $\boldsymbol{y}_k$ can be expressed as

$$(\boldsymbol{y}_0, \boldsymbol{y}_1, \ldots, \boldsymbol{y}_{K-1})(\boldsymbol{I}_K \otimes \boldsymbol{F}_N^* \otimes \boldsymbol{I}_M) = \left(\boldsymbol{d}_0^{\mathrm{r}}, \boldsymbol{d}_1^{\mathrm{r}}, \ldots, \boldsymbol{d}_{J-1}^{\mathrm{r}}\right)\boldsymbol{C}_{\mathrm{a}} + (\boldsymbol{\eta}_0, \boldsymbol{\eta}_1, \ldots, \boldsymbol{\eta}_{K-1}), \tag{12}$$

where $\boldsymbol{C}_{\mathrm{a}}$ is the combined channel matrix,

$$\boldsymbol{C}_{\mathrm{a}} = \begin{pmatrix} \boldsymbol{C}^{0\to 0} & \boldsymbol{C}^{0\to 1} & \cdots & \boldsymbol{C}^{0\to K-1} \\ \boldsymbol{C}^{1\to 0} & \boldsymbol{C}^{1\to 1} & \cdots & \boldsymbol{C}^{1\to K-1} \\ \vdots & \vdots & \ddots & \vdots \\ \boldsymbol{C}^{J-1\to 0} & \boldsymbol{C}^{J-1\to 1} & \cdots & \boldsymbol{C}^{J-1\to K-1} \end{pmatrix}, \tag{13}$$

with $\boldsymbol{C}^{j\to k}$ the delay-Doppler channel matrix from emitter #j to hydrophone #k,

$$\boldsymbol{C}^{j\to k} = \sum_{q=-Q}^{Q} \mathrm{diag}\left(\boldsymbol{C}_{0,q}^{j\to k}, \boldsymbol{C}_{1,q}^{j\to k}, \ldots, \boldsymbol{C}_{N-1,q}^{j\to k}\right)\boldsymbol{Z}_{MN}^{Mq}, \tag{14}$$

$$\boldsymbol{C}_{n,q}^{j\to k} = \begin{pmatrix} h_q^{j\to k}[0] & h_q^{j\to k}[1] & \cdots & h_q^{j\to k}[M-1] \\ W_N^{-n} h_q^{j\to k}[M-1] & h_q^{j\to k}[0] & \cdots & h_q^{j\to k}[M-2] \\ \vdots & \vdots & \ddots & \vdots \\ W_N^{-n} h_q^{j\to k}[1] & W_N^{-n} h_q^{j\to k}[2] & \cdots & h_q^{j\to k}[0] \end{pmatrix}, \tag{15}$$

and $\boldsymbol{\eta}_k$ represents the additive noise component.

The signal processing steps at the Rx can be described as follows:

(i) Combine the received signals $\boldsymbol{y}_k$ and transform the received signal to compute the vector $\boldsymbol{z}$,

$$\begin{aligned} \boldsymbol{z} &= (\boldsymbol{y}_0, \boldsymbol{y}_1, \ldots, \boldsymbol{y}_{K-1})(\boldsymbol{I}_K \otimes \boldsymbol{F}_N^* \otimes \boldsymbol{I}_M) && (16) \\ &= (\boldsymbol{z}_0, \boldsymbol{z}_1, \ldots, \boldsymbol{z}_{K-1}) + (\boldsymbol{\eta}_0, \boldsymbol{\eta}_1, \ldots, \boldsymbol{\eta}_{K-1}), && (17) \end{aligned}$$

where

$$\begin{aligned} \boldsymbol{z}_k &= \sum_{j=0}^{J-1}\left(\boldsymbol{d}_j^{\mathrm{r}} \boldsymbol{C}^{j\to k}\right) && (18) \\ &= \sum_{j=0}^{J-1}\left(\boldsymbol{z}_{\mathrm{p},j,k}^{0\to Q}, \boldsymbol{z}_{j,k,0}, \boldsymbol{z}_{j,k,1}, \ldots, \boldsymbol{z}_{j,k,U-1}, \boldsymbol{z}_{\mathrm{p},j,k}^{-Q\to -1}\right) && (19) \\ &= \left(\boldsymbol{z}_{\mathrm{p},k}^{0\to Q}, \boldsymbol{z}_{k,0}, \boldsymbol{z}_{k,1}, \ldots, \boldsymbol{z}_{k,U-1}, \boldsymbol{z}_{\mathrm{p},k}^{-Q\to -1}\right). && (20) \end{aligned}$$

(ii) Obtain $h_q^{j\to k}[m]$ by channel sensing (using the received pilot blocks, $\boldsymbol{z}_{\mathrm{p},j,k}^{0\to Q}$ and $\boldsymbol{z}_{\mathrm{p},j,k}^{-Q\to -1}$). Specifically, there is a relationship between the pilot block $\boldsymbol{p}_j$ and $\boldsymbol{z}_{\mathrm{p},k}^{0\to Q}$ and $\boldsymbol{z}_{\mathrm{p},k}^{-Q\to -1}$ in (20) as

$$\begin{aligned} \left(\boldsymbol{z}_{\mathrm{p},k}^{-Q\to -1}, \boldsymbol{z}_{\mathrm{p},k}^{0\to Q}\right) &= \sum_{j=0}^{J-1}\left\{\boldsymbol{p}_j\left(\boldsymbol{C}_{0,-Q}^{j\to k}, \boldsymbol{C}_{0,-Q+1}^{j\to k}, \ldots, \boldsymbol{C}_{0,Q}^{j\to k}\right)\right\} && (21) \\ &= \boldsymbol{p}\left(\tilde{\boldsymbol{C}}_{0,-Q}^{k}, \tilde{\boldsymbol{C}}_{0,-Q+1}^{k}, \ldots, \tilde{\boldsymbol{C}}_{0,Q}^{k}\right) + \boldsymbol{\eta}_{\mathrm{p},k}, && (22) \end{aligned}$$

where $\tilde{\boldsymbol{C}}_{0,q}^{k}$ is a circulant matrix, whose elements are the channel impulse responses of length $\tilde{L}$ from all emitters to receiver #k,

$$\tilde{\boldsymbol{C}}_{0,q}^{k} = \begin{pmatrix} h_q^{0\to k}[0] & h_q^{0\to k}[1] & \cdots & h_q^{0\to k}[\tilde{L}-1] & h_q^{1\to k}[0] & h_q^{1\to k}[1] & \cdots & h_q^{1\to k}[\tilde{L}-1] & \cdots & h_q^{J-1\to k}[0] & h_q^{J-1\to k}[1] & \cdots & h_q^{J-1\to k}[\tilde{L}-1] & \mathbf{0}_{1\times(M-J\tilde{L})} \\ h_q^{J-1\to k}[\tilde{L}-1] & h_q^{0\to k}[0] & \cdots & h_q^{0\to k}[\tilde{L}-2] & h_q^{0\to k}[\tilde{L}-1] & h_q^{1\to k}[0] & \cdots & h_q^{1\to k}[\tilde{L}-2] & \cdots & h_q^{J-2\to k}[\tilde{L}-1] & h_q^{J-1\to k}[0] & \cdots & h_q^{J-1\to k}[\tilde{L}-2] & \mathbf{0}_{1\times(M-J\tilde{L})} \\ \vdots & \vdots & \ddots & \vdots & \vdots & \vdots & \ddots & \vdots & \ddots & \vdots & \vdots & \ddots & \vdots & \vdots \\ h_q^{0\to k}[1] & h_q^{0\to k}[2] & \cdots & h_q^{1\to k}[0] & h_q^{1\to k}[1] & h_q^{1\to k}[2] & \cdots & h_q^{2\to k}[0] & \cdots & h_q^{J-1\to k}[1] & h_q^{J-1\to k}[2] & \cdots & h_q^{0\to k}[0] & \mathbf{0}_{1\times(M-J\tilde{L})} \end{pmatrix}, \tag{23}$$

and $\boldsymbol{\eta}_{\mathrm{p},k}$ is an approximation error. This approximation comes from the fact that we ignore the latter part of the channel impulse response as we assume that $\left(h_q^{j\to k}[0], h_q^{j\to k}[1], \ldots, h_q^{j\to k}[L-1]\right) \simeq \left(h_q^{j\to k}[0], h_q^{j\to k}[1], \ldots, h_q^{j\to k}[\tilde{L}-1], \mathbf{0}_{1\times(L-J\tilde{L})}\right)$. By this assumption, (22) can be obtained from (2) and (21) as,

$$
\begin{aligned}
\sum_{j=0}^{J-1} \left\{ \boldsymbol{p}_j \left(\boldsymbol{C}_{0,-Q}^{j\to k}, \boldsymbol{C}_{0,-Q+1}^{j\to k}, \ldots, \boldsymbol{C}_{0,Q}^{j\to k} \right) \right\} &\simeq \sum_{j=0}^{J-1} \left\{ \boldsymbol{p}_j \left(\tilde{\boldsymbol{C}}_{0,-Q}^{j\to k}, \tilde{\boldsymbol{C}}_{0,-Q+1}^{j\to k}, \ldots, \tilde{\boldsymbol{C}}_{0,Q}^{j\to k} \right) \right\} && (24)\\
&= \sum_{j=0}^{J-1} \left\{ \boldsymbol{p} \left(\boldsymbol{Z}_M \right)^{j\tilde{L}} \left(\tilde{\boldsymbol{C}}_{0,-Q}^{j\to k}, \tilde{\boldsymbol{C}}_{0,-Q+1}^{j\to k}, \ldots, \tilde{\boldsymbol{C}}_{0,Q}^{j\to k} \right) \right\} && (25)\\
& && (26)\\
&= \boldsymbol{p} \left(\tilde{\boldsymbol{C}}_{0,-Q}^{k}, \tilde{\boldsymbol{C}}_{0,-Q+1}^{k}, \ldots, \tilde{\boldsymbol{C}}_{0,Q}^{k} \right), && (27)
\end{aligned}
$$

where $\tilde{\boldsymbol{C}}_{0,q}^{j\to k}$ is a matrix given by

$$
\begin{aligned}
\tilde{\boldsymbol{C}}_{0,q}^{j\to k} &= \left.\boldsymbol{C}_{0,q}^{j\to k}\right|_{h_q^{j\to k}[m]=0\ (m\geq\tilde{L})} && (28)\\
&= \begin{pmatrix}
h_q^{j\to k}[0] & h_q^{j\to k}[1] & \cdots & h_q^{j\to k}[\tilde{L}-1] & 0 & 0 & \cdots & 0\\
0 & h_q^{j\to k}[0] & \cdots & h_q^{j\to k}[\tilde{L}-2] & h_q^{j\to k}[\tilde{L}-1] & 0 & \cdots & 0\\
\vdots & \vdots & \ddots & \vdots & \vdots & \vdots & \ddots & \vdots\\
h_q^{j\to k}[1] & h_q^{j\to k}[2] & \cdots & 0 & 0 & 0 & \cdots & h_q^{j\to k}[0]
\end{pmatrix}. && (29)
\end{aligned}
$$

Hence, the Rx obtains $h_q^{j\to k}[m]\left(m \leq \tilde{L}-1\right)$ by calculating (22).

(iii) Obtain message $\boldsymbol{m}_{j,u}$ by equalization. Specifically, there is a relationship between the message block $\boldsymbol{m}_{j,u}$ and $\boldsymbol{z}_{k,u}$ in (20) as

$$
\begin{aligned}
\left(\boldsymbol{z}_{0,u}, \boldsymbol{z}_{1,u}, \ldots, \boldsymbol{z}_{K-1,u}\right) &= \left(\boldsymbol{m}_{0,u}, \boldsymbol{m}_{1,u}, \ldots, \boldsymbol{m}_{J-1,u}\right) \boldsymbol{C}_{\mathrm{cu}} && (30)\\
&= \left(\boldsymbol{m}_{0,u}, \boldsymbol{m}_{1,u}, \ldots, \boldsymbol{m}_{J-1,u}\right) \begin{pmatrix}
\boldsymbol{C}_{\mathrm{cu}}^{0\to 0} & \boldsymbol{C}_{\mathrm{cu}}^{0\to 1} & \cdots & \boldsymbol{C}_{\mathrm{cu}}^{0\to K-1}\\
\boldsymbol{C}_{\mathrm{cu}}^{1\to 0} & \boldsymbol{C}_{\mathrm{cu}}^{1\to 1} & \cdots & \boldsymbol{C}_{\mathrm{cu}}^{1\to K-1}\\
\vdots & \vdots & \ddots & \vdots\\
\boldsymbol{C}_{\mathrm{cu}}^{J-1\to 0} & \boldsymbol{C}_{\mathrm{cu}}^{J-1\to 1} & \cdots & \boldsymbol{C}_{\mathrm{cu}}^{J-1\to K-1}
\end{pmatrix}, && (31)
\end{aligned}
$$

where

$$
\boldsymbol{C}_{\mathrm{cu}}^{j\to k} = \begin{pmatrix}
\boldsymbol{C}_{\tilde{u},-Q}^{j\to k} & \boldsymbol{C}_{\tilde{u},-Q+1}^{j\to k} & \cdots & \boldsymbol{C}_{\tilde{u},Q-1}^{j\to k} & \boldsymbol{C}_{\tilde{u},Q}^{j\to k} & \mathbf{0}_{M\times M} & \cdots & \mathbf{0}_{M\times M}\\
\mathbf{0}_{M\times M} & \boldsymbol{C}_{\tilde{u}+1,-Q}^{j\to k} & \cdots & \boldsymbol{C}_{\tilde{u}+1,Q-2}^{j\to k} & \boldsymbol{C}_{\tilde{u}+1,Q-1}^{j\to k} & \boldsymbol{C}_{\tilde{u}+1,Q}^{j\to k} & \cdots & \mathbf{0}_{M\times M}\\
\vdots & \vdots & \ddots & \vdots & \vdots & \vdots & \ddots & \vdots\\
\mathbf{0}_{M\times M} & \mathbf{0}_{M\times M} & \cdots & \mathbf{0}_{M\times M} & \boldsymbol{C}_{\tilde{u}+P-1,-Q}^{j\to k} & \boldsymbol{C}_{\tilde{u}+P-1,-Q+1}^{j\to k} & \cdots & \boldsymbol{C}_{\tilde{u}+P-1,Q}^{j\to k}
\end{pmatrix}, \qquad (32)
$$

and $\tilde{u} = (1+2Q) + u(P+2Q)$.

Hence, the Rx calculates $\tilde{\boldsymbol{C}}_{\mathrm{cu}} = \left.\boldsymbol{C}_{\mathrm{cu}}\right|_{h_q^{j\to k}[m]=0\ (m\geq\tilde{L})}$ using $h_q^{j\to k}[m]\left(m \leq \tilde{L}-1\right)$ and obtains the received message $\boldsymbol{r}_{j,u}$ as

$$
\begin{aligned}
\left(\boldsymbol{r}_{0,u}, \boldsymbol{r}_{1,u}, \ldots, \boldsymbol{r}_{J-1,u}\right) &= \left[\left(\boldsymbol{z}_{0,u}, \boldsymbol{z}_{1,u}, \ldots, \boldsymbol{z}_{K-1,u}\right) + \left(\boldsymbol{\eta}_{0,u}, \boldsymbol{\eta}_{1,u}, \ldots, \boldsymbol{\eta}_{K-1,u}\right)\right] \tilde{\boldsymbol{C}}_{\mathrm{cu}}^{*} \left(\tilde{\boldsymbol{C}}_{\mathrm{cu}} \tilde{\boldsymbol{C}}_{\mathrm{cu}}^{*}\right)^{-1} && (33)\\
&= \left(\boldsymbol{m}_{0,u}, \boldsymbol{m}_{1,u}, \ldots, \boldsymbol{m}_{J-1,u}\right) + \left(\tilde{\boldsymbol{\eta}}_{0,u}, \tilde{\boldsymbol{\eta}}_{1,u}, \ldots, \tilde{\boldsymbol{\eta}}_{J-1,u}\right). && (34)
\end{aligned}
$$

where $\boldsymbol{\eta}_{k,u}$ is a part of $\boldsymbol{\eta}_k$. Notice that $\tilde{\boldsymbol{\eta}}_{j,u}$ is a sum of three noises; part of the additive noise, approximation error in step (iii), and the channel measurement noise (if an estimated channel is used).

Note that the above signal processing steps are based on the following assumptions.

- All transmitted signals reach the Rx at the same time.
- The Doppler shift is the same for all the Tx-Rx pairs.

In simulations (Section III), we will consider the communication quality of MIMO systems if there exist time- and frequency-lags between the significant paths.

D. Characteristics of MIMO D-OSDM

In this paper, we employ normal D-OSDM and MIMO D-OFDM as main benchmarks. First, we briefly discuss our MIMO D-OSDM in comparison to the existing normal D-OSDM approach. The advantage of MIMO D-OSDM is an improvement of the spectrum efficiency; it can improve the spectrum efficiency J times that of normal D-OSDM while almost preserving its resilience against delay and Doppler spread without employing a higher modulation rate (e.g., QPSK to 16QAM) that is sensitive to channel noise. On the other hand, the disadvantage of MIMO D-OSDM is an increase of noise in the received

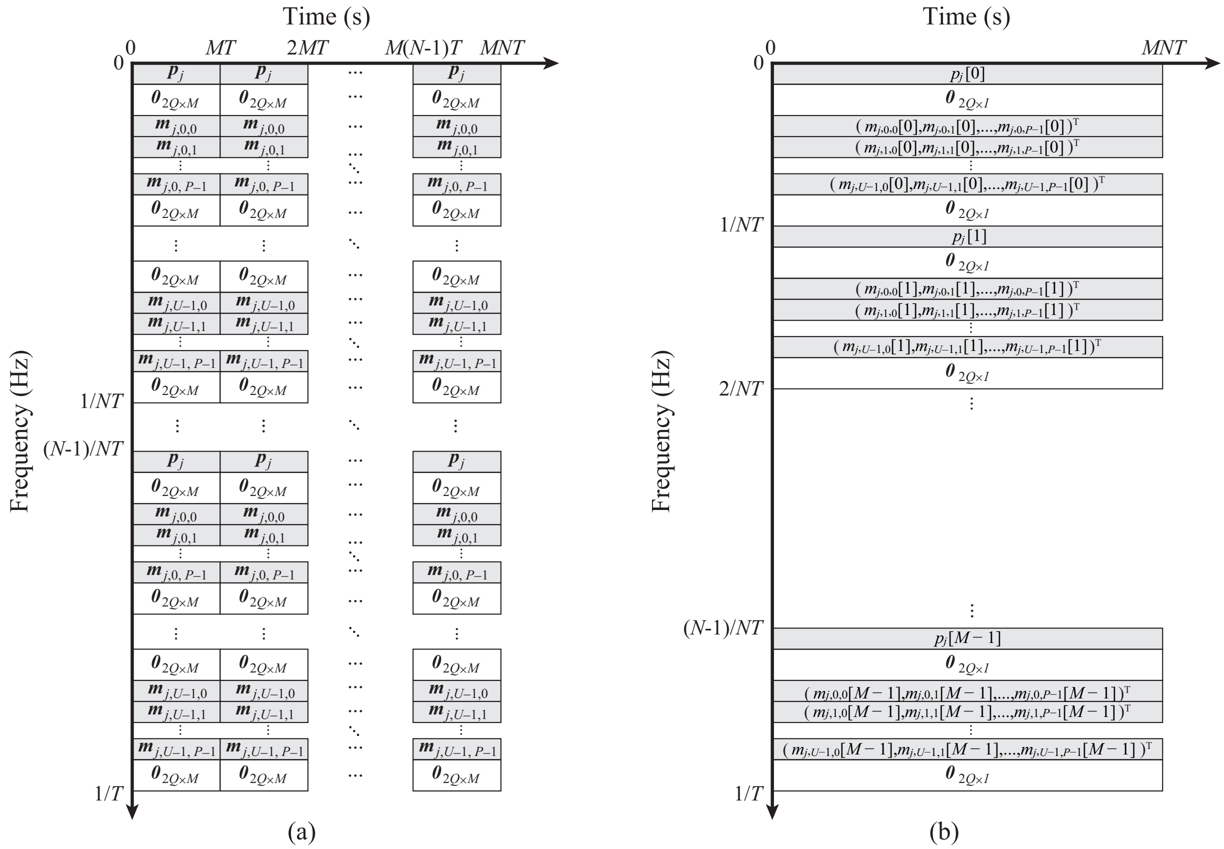

Fig. 4. Structure of (a) MIMO D-OSDM signal and (b) MIMO D-OFDM signal in the time-frequency domain.

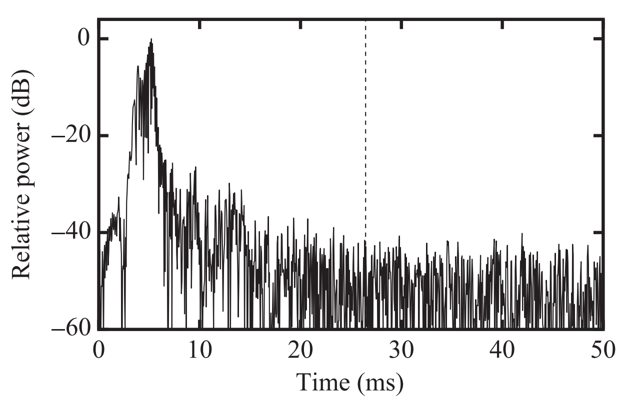

Fig. 5. Channel impulse response obtained at Suruga Bay (Tx-Rx distance: 350 m).

message, since the measurable delay spread of MIMO D-OSDM is limited compared to normal D-OSDM, as described in Section II-C. Specifically, MIMO D-OSDM measures $h_q^{j\to k}[m]$ for $0 \le m \le \tilde{L}-1$ and assumes $h_q^{j\to k}[m] = 0$ for $m \ge \tilde{L}$. Hence, MIMO D-OSDM can be extended to larger architectures, but the maximum tolerated delay spread is inversely proportional to the number of senders. In other words, the communication speed increases proportional to the number of senders, but the communication quality becomes worse. However, the increase of noise due to the above assumption remains small when the number of senders J is small, since the average power of the channel impulse response decays with the delay, as shown in Fig. 5. In the following sections, we show that the advantages of MIMO D-OSDM outweigh its disadvantages when $J = 2$.

We also briefly discuss our MIMO D-OSDM in comparison to the existing MIMO D-OFDM approach. Fig. 4(a) shows the signal structure of the MIMO D-OSDM signal (emitted from a specific emitter #j) in the time-frequency domain, where T represents the symbol time. As shown in the figure, the data matrix $\boldsymbol{D}_j$ periodically appears in the MIMO D-OSDM signal in the time-frequency domain. Focusing on the structure of the MIMO D-OSDM signal in the frequency domain, there are MN subcarriers with M pilot subcarriers and U groups of P data subcarriers. Both pilot and data subcarrier groups are separated using $2Q+1$ null subcarriers. In that sense, the MIMO D-OSDM signal is comparable to the MIMO OFDM signal that also separates data subcarrier groups from pilot subcarriers using null subcarriers (MIMO D-OFDM), as shown in Fig. 4(b).

In [24], we showed that normal D-OSDM has advantages over normal D-OFDM [11], [12], [13] in terms of the low dynamic range of the transmitted signal and a better communication quality, in exchange for receiver complexity. These advantages and disadvantages still hold true when we compare MIMO D-OSDM and MIMO D-OFDM. Let us first focus on the peak-to-average power ratio (PAPR) of these signals. The maximum PAPR of the MIMO D-OSDM signal is proportional to the total number of message and pilot blocks $(1+PU)$, while that of the MIMO D-OFDM signal is proportional to the total number of active subcarriers $M(1+PU)$. Hence, MIMO D-OSDM is attractive from a practical point of view, since a small PAPR can avoid problems derived from the nonlinearity of the signal power amplifier at the Tx. Next let us focus on the delay and Doppler resilience of these signals. In both techniques, the null subcarriers between the pilot and data signals are used to facilitate Doppler compensation by avoiding ICI. On the other hand, comparing Figs. 4(a) and 4(b), it is clear that both the message and pilot signals appear periodically in both the time and frequency domains in the MIMO D-OSDM signal, while they appear at unique subcarriers in the MIMO D-OFDM signal. This periodical appearance of pilot and data signals in MIMO D-OSDM provides a robustness against frequency-selective fading, hence, MIMO D-OSDM would achieve better communication quality than MIMO D-OFDM in a UWA channel with a large delay spread. Note that such spreading the information in this way is not unique to OSDM; it can be done with multiple frequency-shift keying (MFSK) [31] and [15] does it with OFDM.

III. Performance Evaluation in Simulations

A. Simulation environment

TABLE III
Parameters of normal D-OSDM, MIMO D-OSDM, classical MIMO OFDM and MIMO D-OFDM used in simulation I.

<table>
<tr><th></th><th>Normal D-OSDM</th><th>MIMO D-OSDM</th><th>MIMO D-OFDM</th><th>Classical MIMO-OFDM</th></tr>
<tr><td>M</td><td colspan="4">127</td></tr>
<tr><td>P</td><td colspan="3">2</td><td>1</td></tr>
<tr><td>U</td><td colspan="3">1</td><td>1</td></tr>
<tr><td>Q</td><td colspan="3">2</td><td>0</td></tr>
<tr><td>L</td><td colspan="4">127</td></tr>
<tr><td>J</td><td>1</td><td colspan="3">2</td></tr>
<tr><td>K</td><td colspan="4">2</td></tr>
<tr><td>Modulation
(b: Number of bits per symbol)</td><td>16QAM
($b=4$)</td><td colspan="3">QPSK ($b=2$)</td></tr>
<tr><td>Channel coding
(R: Code rate)</td><td colspan="4">N/A ($R=1$)</td></tr>
<tr><td>Carrier frequency f_c (kHz)</td><td colspan="4">24</td></tr>
<tr><td>Signal bandwidth B (kHz)</td><td colspan="4">4.8</td></tr>
<tr><td>Effective data rate (kbps)
$bJMPUBR/(MN+L)$</td><td colspan="3">3.20</td><td>6.40</td></tr>
<tr><td>Spectrum efficiency (bps/Hz)
$bJMPUR/(MN+L)$</td><td colspan="3">0.66</td><td>1.33</td></tr>
</table>

In this section, we evaluate the performance of MIMO D-OSDM in simulations. In simulation I, we evaluated the performance [output signal-to-noise ratio (OSNR) and bit-error-rate (BER)] of MIMO D-OSDM, normal D-OSDM, MIMO D-OFDM and classical MIMO OFDM in an UWA channel with various f_d values at a specific E_b/N_0 of 25 dB. In simulation II, we evaluated the BER of MIMO D-OSDM, normal D-OSDM and MIMO D-OFDM in an UWA channel with various E_b/N_0 values at a specific f_d of 8 Hz. In simulation III, we evaluated the OSNR and BER of MIMO D-OSDM and MIMO D-OFDM in an UWA channel at a specific E_b/N_0 of 15 dB and f_d of 8 Hz, with time- and frequency-lags of the significant paths (Δt and Δf).

Table III shows the parameters used in simulation I. We consider MIMO D-OSDM with two emitters and two hydrophones (2×2). We also consider normal D-OSDM with a single emitter and two hydrophones (1×2), as well as MIMO D-OFDM and classical MIMO OFDM with two emitters and two hydrophones (2×2) as references. Note that the signal bandwidth, data rate, and total output power of the MIMO D-OSDM, normal D-OSDM, and MIMO D-OFDM are the same, while the data rate of classical MIMO OFDM is double to those of Doppler-resilient schemes (MIMO D-OSDM, normal D-OSDM and MIMO D-OFDM).

TABLE IV
PARAMETERS OF NORMAL D-OSDM, MIMO D-OSDM, AND MIMO D-OFDM USED IN SIMULATION II AND III , AND EXPERIMENTS.

	Normal D-OSDM	MIMO D-OSDM	MIMO D-OFDM
M	127		
P	2		
U	1		
Q	2		
L	127		
J	1	2	
K	2		
Modulation (b: Number of bits per symbol)	16QAM (b = 4)	QPSK (b = 2)	
Channel coding (R: Code rate)	Turbo code ($R = 1/3$)		
Carrier frequency f_c (kHz)	24		
Signal bandwidth B (kHz)	4.8		
Effective data rate (kbps) $bJMPUBR/(MN + L)$	1.06 (with coding) 3.20 (without coding)		
Spectrum efficiency (bps/Hz) $bJMPUR/(MN + L)$	0.22 (with coding) 0.66 (without coding)		

Table IV shows the parameters used in simulations II and III. Different from simulation I, we do not employ classical MIMO OFDM since the performance of MIMO OFDM was not good in UWA channels with large Doppler spread. Hence, we consider MIMO D-OSDM with two emitters and two hydrophones (2×2), and consider normal D-OSDM with a single emitter and two hydrophones (1×2), as well as MIMO D-OFDM with two emitters and two hydrophones (2×2) as references. Note that the signal bandwidth, data rate, and total output power of MIMO D-OSDM, normal D-OSDM, and MIMO D-OFDM are the same. Furthermore, a Turbo code with a code rate R of 1/3 is employed in simulations II and III, to evaluate the performance of communication schemes in practical circumstances. The channel encoding is performed block-by-block so that the input block length to the encoder is the same for D-OSDM, MIMO D-OSDM, and MIMO D-OFDM. Specifically,

1) The transmitter reads binary data of length 328 bits.
2) The transmitter calculates the encoded message of length $328 \times 3 + 12$ (tail bits) = 996 bits using the considered Turbo code (code rate R: 1/3).
3) For the 2×2 MIMO system (MIMO D-OSDM and MIMO D-OFDM), the transmitter calculates 498 QPSK symbols from 996 bits, adds 10 redundant symbols to generate a symbol length of 508 ($JMPU$). Note that the redundant symbols are not used to calculate the BER.
4) For the 2×1 MISO system (Normal D-OSDM), the transmitter calculates 249 16QAM symbols from 996 bits, adds 5 redundant symbols to generate a symbol length of 254 ($JMPU$). Note that the redundant symbols are again not used to calculate the BER.
5) These $JMPU$ symbols are then converted to vectors $\boldsymbol{m}_{j,u,p}$ of size $1 \times M$.
6) Finally, the transmitter calculates $\boldsymbol{x}_0, \boldsymbol{x}_1, \ldots, \boldsymbol{x}_{J-1}$ and $\boldsymbol{x}_0^{\mathrm{OFDM}}, \boldsymbol{x}_1^{\mathrm{OFDM}}, \ldots, \boldsymbol{x}_{J-1}^{\mathrm{OFDM}}$ from $\boldsymbol{m}_{j,u,p}$, and outputs them to the UWA channel.

In simulations, a discrete-time equivalent baseband channel model was established with a maximum delay of 127 taps (26.4 ms) and a maximum Doppler spread of f_d Hz taking various values, to simulate an UWA channel with large delay and Doppler spreads. The first path exhibits a Rice distribution with Rice factor (the ratio of signal power in dominant component over the scattered power) of 0 dB, considering the fact that the experiment was performed in a line-of-sight environment, where the direct-path signal and surface-reflected signal arrive within a symbol time. Other paths exhibit a Rayleigh distribution where the gain of the discrete paths decreased 0.31 dB per tap in power. In such condition, the root-mean square (RMS) delay spread of the channel was about 5 ms (approximately 25 symbols) [32]. The channel impulse responses from emitter #j to hydrophone #k were independent of each other. The Doppler spectrum was assumed to have a bell shape with a maximum Doppler shift of f_d Hz. A Gaussian white process was used as additive noise.

B. Results of Simulations I and II

Let us focus on the result of simulation I (Fig. 6). Figs. 6(a) and 6(b) show the relationship between the normalized maximum Doppler shift (ratio of f_d to subcarrier spacing) and the OSNR and BER without coding, respectively. Note that the OSNR is the ratio of the average reference signal power to the mean square error. It is computed by measuring the modulation accuracy by comparing the received symbol constellation with the ideal input signal (reference constellation). Specifically, the OSNR is calculated as

$$OSNR = \frac{\sum_{j=0}^{J-1}\sum_{m=0}^{M-1}\sum_{p=0}^{P-1}\sum_{u=0}^{U-1}|M_{j,u}[p,m]|^2}{\sum_{j=0}^{J-1}\sum_{m=0}^{M-1}\sum_{p=0}^{P-1}\sum_{u=0}^{U-1}|M_{j,u}[p,m]-\tilde{M}_{j,u}[p,m]|^2}, \tag{35}$$

where $\tilde{M}_{j,u}[p,m]$ and $M_{j,u}[p,m]$ are the received symbol constellation and ideal input signal (reference constellation), respectively.

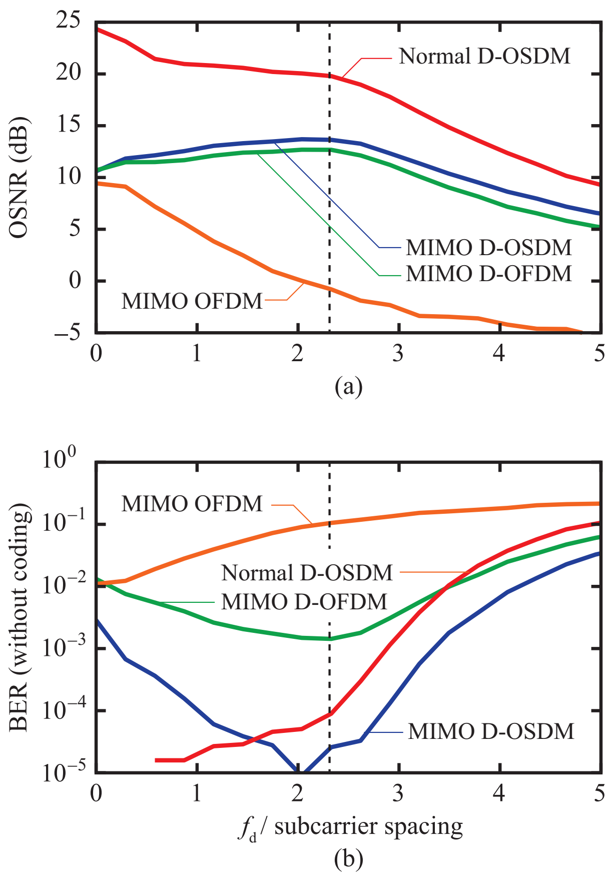

Fig. 6. Results of simulation I: Relationship between the normalized maximum Doppler shift and (a) OSNR and (b) BER without coding.

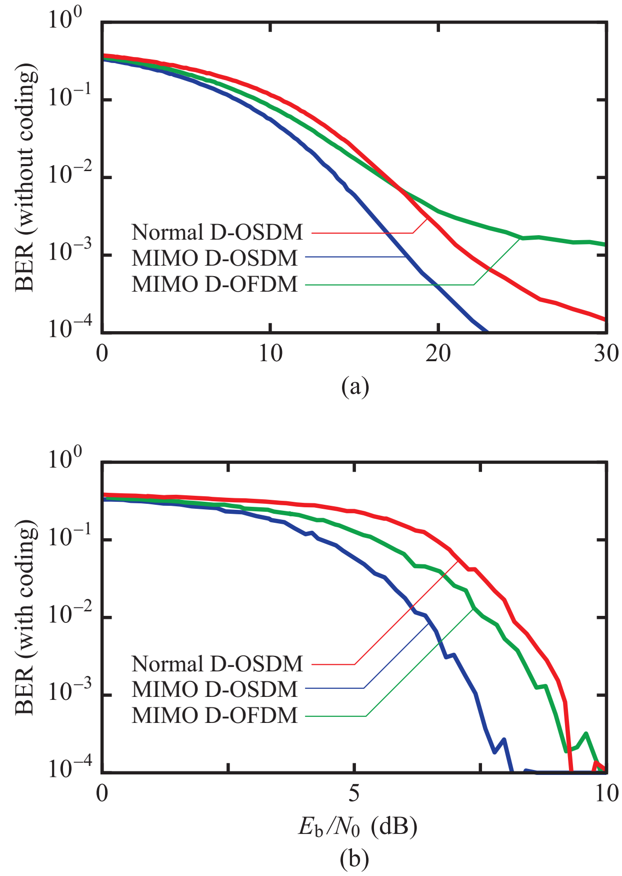

Fig. 7. Results of simulation II: Relationship between the E_b/N_0 and (a) BER without coding and (b) BER with coding.

As shown in Fig. 6(a), classical MIMO OFDM performs best without any Doppler spread, and the OSNR curve of classical MIMO OFDM is a monotonically decreasing function. This is because the Doppler factor becomes noise to the classical MIMO OFDM scheme due to ICI. Different from classical MIMO OFDM, the decrease of the OSNR of normal D-OSDM is suppressed until the normalized Doppler shift is about 2.4 times larger than the subcarrier spacing (as indicated by the dotted line in Fig. 6). Furthermore, the OSNR curves of MIMO D-OSDM and MIMO D-OFDM have a local maximum at the dotted line, respectively. This is because they can utilize both the delay and Doppler diversity as f_d increases, but if f_d is too high it causes interference between the pilot and data subcarriers.

Focusing on the BER curves of MIMO D-OSDM, normal D-OSDM, MIMO D-OFDM, and classical MIMO OFDM at the dotted line in Fig. 6(b), it is clear that MIMO D-OSDM achieves a better performance than the benchmarks [1]. As shown in

[1]Note that the BER curves cross one another, but not the OSNR curves in Fig. 6. This is because we employ different symbol constellations in the red, green, blue and orange lines. In this paper, we compare 16 QAM (red line, sensitive to noise, fast) with one transmit antenna and QPSK (green, blue and orange lines, robust to noise, slow) with two transmit antennas resulting in the same effective data rate. Hence, the relationship between OSNR and the BER of 16QAM (red line) and QPSK (blue, green and orange lines) is different, resulting in a different tendency for the two graphs.

the figure, MIMO D-OSDM achieves a BER of 2.5×10^{-5} at the dotted line, while normal D-OSDM, MIMO D-OFDM and classical MIMO OFDM achieve a BER of 5.6×10^{-5}, 1.4×10^{-3} and 9.0×10^{-2} at the same Doppler shift, respectively.

Let us next focus on the result of simulation II (Fig. 7). Figs. 7(a) and 7(b) show a relationship between the E_{b}/N_0 and BER with/without coding, respectively, when the normalized Doppler shift is about 2.4 times larger than the subcarrier spacing (f_{d} = 8 Hz). As shown in Fig. 7(a), MIMO D-OSDM achieves a BER of 10^{-3} when E_{b}/N_0 is 18.0 dB, while normal D-OSDM achieves the same BER when E_{b}/N_0 is 22.0 dB and MIMO D-OFDM has a BER floor above 10^{-3}. The advantage of MIMO D-OSDM over normal D-OSDM and MIMO D-OFDM still holds true when we compare them with channel coding. As shown in Fig. 7(b), MIMO D-OSDM achieves a BER of 10^{-3} when E_{b}/N_0 is 7.4 dB, while normal D-OSDM and MIMO D-OFDM achieve the same BER when E_{b}/N_0 is 8.7 dB and 9.1 dB, respectively.

These simulation results suggest that MIMO D-OSDM is attractive for UWA communication. From simulation I, we found that MIMO D-OSDM, normal D-OSDM, and MIMO D-OFDM achieve better performance than classical MIMO OFDM under the presence of Doppler spread. In UWA communication, the channel diversity can enhance the communication system performance, while the noise limits the communication system performance. Since MIMO D-OSDM, normal D-OSDM, and MIMO D-OFDM have null subcarriers to safeguard against ICI, they can utilize the Doppler factor to give the communication system channel diversity, resulting in a better performance than classical schemes under the presence of Doppler spread [33]. Furthermore, from simulations I and II, we found that the performance of MIMO D-OSDM is better than normal D-OSDM and MIMO D-OFDM. This means that the advantages of MIMO D-OSDM (increase of spectrum efficiency without using a higher modulation rate) outweigh its disadvantage (an increase of noise due to channel approximation), as described in Section II-D. In addition, the resilience of MIMO D-OSDM with respect to the delay spread is better than that of MIMO D-OFDM, as described in Section II-D. These advantages of MIMO D-OSDM were also validated in the following experiments.

C. Results of Simulation III

Let us next focus on the result of simulation III. In simulation III, we evaluated the OSNR and BER of MIMO D-OSDM and MIMO D-OFDM in an UWA channel with time- and frequency-lags between the significant paths. Fig. 8(a) shows a scenario when there exist a time-lag between significant paths. As shown in the figure, there are four significant paths between the Tx and Rx (E#0 → H#0, E#0 → H#1, E#1 → H#0 and E#1 → H#1), and the spatial position difference between emitters and hydrophones causes a different time-of-arrival (in this figure, the transmitted signals passing through E#1 → H#0 and E#1 → H#1 arrive at the Rx with a delay of Δt compared to the signals passing through E#0 → H#0 and E#0 → H#1). Fig. 9(a) shows a scenario when there exist a frequency-lag between significant paths. As shown in the figure, the Doppler shift of each path differs due to the movement of the communication platform (in this figure, E#1 → H#0 and E#1 → H#1 have a Doppler shift of Δf compared to that passes through E#0 → H#0 and E#0 → H#1).

Figs. 8(b) and (c) show the relationship between Δt and the OSNR and BER with coding, respectively. From these figures, we found that a small time-lag between the received signals does not affect the performance of the MIMO system much. As shown in Fig. 8(b), the OSNR curves of MIMO D-OSDM and MIMO D-OFDM gradually decrease as the time-lag between the two received signals increases, and suddenly drops when Δt exceeds the maximum tolerated delay spread [$L/(JB)$]. However, as shown in Fig. 8(c), the BER remains under 10^{-4} when Δt remains within 10 ms. Hence, a time-lag among the received signals does not affect the performance of a MIMO system much, since a Δt of 10 ms already corresponds to a length difference of 15 m. However, it was also found that an extension to larger architectures and an increase of bandwidth (increase of J and B, respectively) limits the allowable time-lag, and a careful design of the Tx and Rx (e.g., physical arrangement of emitters and hydrophones) is necessary.

Figs. 9(b) and (c) show the relationship between Δf and the OSNR and BER with coding, respectively. As before, the OSNR curves of MIMO D-OSDM and MIMO D-OFDM gradually decrease as the frequency-lag between the two received signals increases, and the BER remains under 10^{-4} when Δf remains within two subcarrier spacings [$2B/(MN)$ = 6.2 Hz]. From these results, it was found that the effect of frequency-lag among the received signals may affect the performance of a MIMO system, since the rotational movement of the communication platform can easily exceed the allowable frequency lag for practical parameter values. Specifically, a velocity difference Δv of 0.4 m/s between E#0 and E#1 creates a Δf of two subcarrier spacings when we use the parameters shown in Table IV, where

$$\Delta v = c\frac{\Delta f}{f_{\mathrm{c}} + \Delta f}, \tag{36}$$

and c is the sound velocity in water (approximately 1,500 m/s). However, considering the facts that the rudder of underwater vehicles has a deflection to avoid stalling and the turning radius increases as the speed increases [34], such a maneuver that generates a large velocity difference between emitters or hydrophones and thus a performance degradation remains rare in actual underwater vehicle operations. Of course a careful design of the Tx and Rx (e.g., parameters M, N and B) is necessary, since an increase of M and N and a decrease of signal bandwidth B makes the subcarrier spacing small, and an increase of the carrier frequency makes the Doppler difference Δf large, which all limit the allowable frequency lag.

These simulation results suggest that MIMO D-OSDM is attractive for UWA communication, but careful consideration is necessary since the communication quality of MIMO systems drops if there exist time- and frequency-lags of the significant

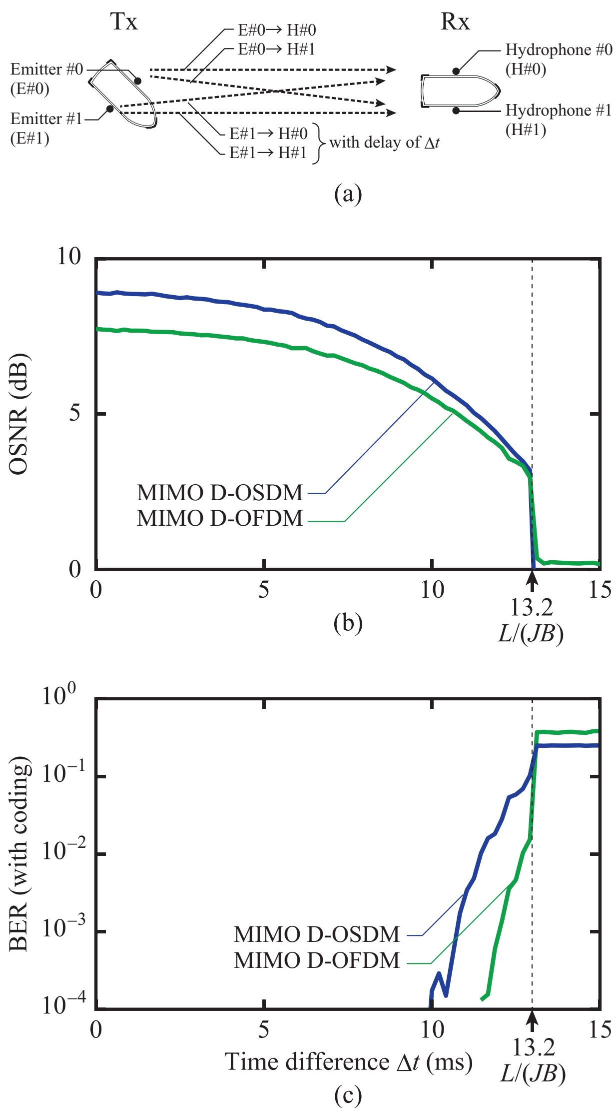

Fig. 8. Results of simulation III: (a) Simulation scenario and relationship between the time-lag Δt between significant paths and (b) OSNR and (c) BER without coding.

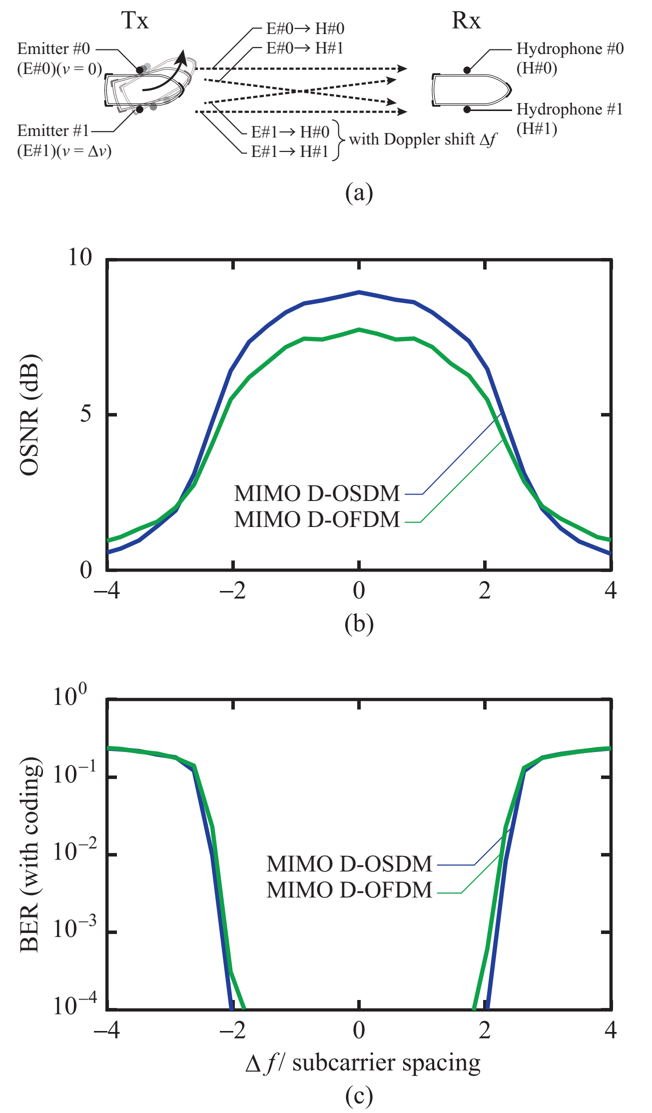

Fig. 9. Results of simulation III: (a) Simulation scenario and relationship between the frequency-lag Δf between received signals and (b) OSNR and (c) BER without coding.

paths. Especially, the effect of a frequency-lag among the received signals may affect the performance of a MIMO system, since the rotational movement of the communication platform can exceed the allowable frequency-lag easily for practical parameter values (Table IV). Such effects were also validated in the following experiments.

IV. Performance Evaluation in Sea Trials

A. Experimental setup and procedure

In this section, we evaluate the performance of MIMO D-OSDM in sea trials. The experiment was performed in the Suruga Bay, Japan (35.02° N, 138.89° E) on 22 June 2018. Figs. 10 and 11 show the experimental setup. As shown in the figures, the Tx and Rx are mounted on a research vessel and a floating barge, respectively. At the Tx, two emitters (OST-2120, OKI SEATEC) were fixed 2.0 m below the water level using a stainless tube, and the distance between emitters was about 3.2 m. At the Rx, two hydrophones (OST-2120, OKI SEATEC) were hung 12.4 m below the water level, and the distance between hydrophones was about 3.0 m. The water depth at the Rx was 32 m, and it increases up to 54 m as the Tx-Rx distance increases. The position and velocity of the Tx were monitored by a GPS receiver throughout the experiment.

During the sea trial, the research vessel with the Tx makes round-trips between the starting point and turning point (Fig. 12). Specifically, the round-trip was performed by the following steps.

Step 1: The Tx starts emitting the signal

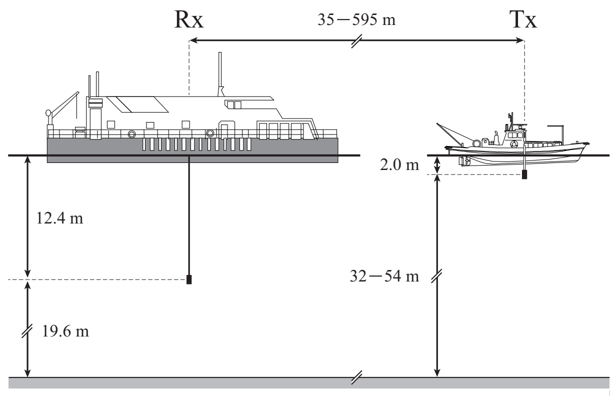

Fig. 10. Side view of the transmitter and receiver.

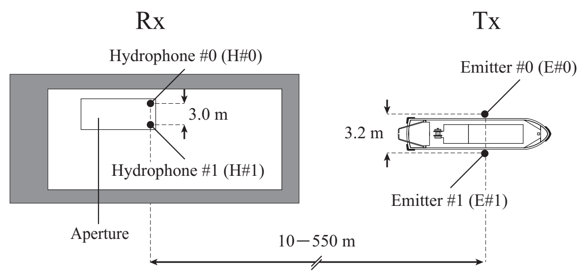

Fig. 11. Top view of the transmitter and receiver.

Step 2: The Tx departs the starting area located 35 m from the Rx and runs toward the turning area with constant speed.

Step 3: When the Tx approaches the turning area located 550 m from the Rx, the Tx decreases its speed, changes its direction and runs toward the starting area with constant speed.

Step 4: When the Tx approaches the starting area, the Tx decreases its speed, changes its direction and stops emitting the signal.

The sea trial was divided into two parts – channel probing and testing the UWA communication. In the channel probing, we measured the delay and Doppler spreads of the UWA channel. As probing signal, two signals – a burst chirp signal (center frequency: 24 kHz, bandwidth: 4.8 kHz) and a continuous sinusoid of 24 kHz – are employed to measure the delay and Doppler spread, respectively. The above round-trip was repeated two times for each signal.

To test the UWA communication, we emitted MIMO D-OSDM, normal D-OSDM and MIMO D-OFDM signals with parameters as in Table III. Different from the simulation that is performed using baseband signals, the experiment was performed

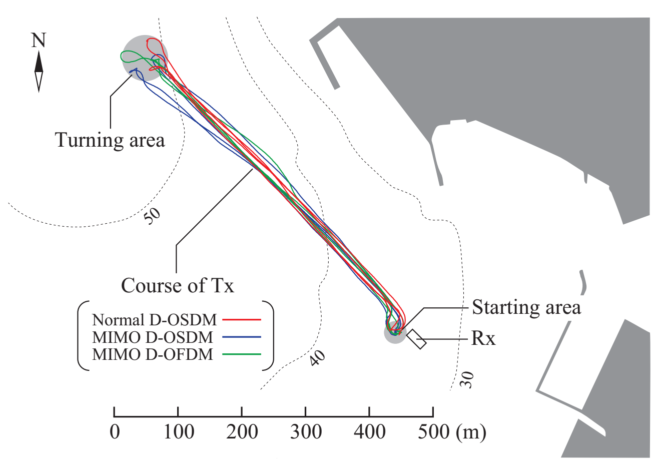

Fig. 12. Map of the sea trial area.

using passband signals whose center frequency was 24 kHz. As for channel probing, the Tx made two round-trips for each signal. During the round-trips, the Tx outputs 36 signal blocks 49 times (in total: 1,764 signal blocks) with an interval of 30 s for each signal. The Rx recorded the signal, performed the Doppler shift correction, performed the signal demodulation, and calculated the E_b/N_0 and output BER of the received signal. Specifically, the Rx removes the overall Doppler shift prior to the signal demodulation in the following two steps: (1) rough Doppler shift correction using measured velocity of the Tx by the GPS and (2) precise Doppler shift correction by minimizing the spillover energy in null subcarriers block-by-block. Furthermore, the E_b/N_0 is calculated by measuring the signal-to-noise ratio (SNR) under the following assumptions on the communication signal and noise:

1) During the sea trial, the transmitter outputs 36 signal blocks 49 times with an interval of 30 s for each signal. We call a group of 36 signal blocks as frame.
2) The receiver firstly calculates the mean power of each received signal block (with a bandpass filter whose cutoff frequencies are 21.5 and 26.5 kHz) and stores it as $S_{n_b,n_r} + N_{n_b,n_r}$, where $n_b = 0, 1, \ldots, 35$ (block number) and $n_r = 0, 1, \ldots, 48$ (frame number).
3) Then the receiver calculates the mean power of the noise from the recorded signal and stores it as $\tilde{N}_{n_r}$ when the transmitter is not active.
4) The SNR of each signal block is calculated as $(S_{n_b,n_r} + N_{n_b,n_r} - \tilde{N}_{n_r})/\tilde{N}_{n_r}$.
5) Finally, the E_b/N_0 is calculated by dividing the SNR by the (effective) spectrum efficiency, as shown in Table III.

In experiments, the distance between transmitters / hydrophones was set as 3.2 m and 3.0 m, respectively. In this case, the maximal time-lag Δt in Section III-C becomes approximately 4 ms, when the Tx changes its direction at the starting and turning areas (path length from E#0 and E#1 to the Rx differs 3.2 m at most). Since the length of the guard interval was 26.5 ms, such a time-lag does not affect the communication quality much.

B. *Results of channel probing*

Fig. 13 shows the results of channel probing. Let us focus on the results obtained by GPS [Figs. 13(a) and 13(b)], that show the relationship of the experiment time with the Tx-Rx distance and speed of the Tx, respectively. As shown in Fig. 13(a), the Tx makes two round trips between the starting area (Tx-Rx distance: 35 m) and turning area (Tx-Rx distance: 550 m) for 26 min. As shown in Fig. 13(b), the Tx runs between the starting area and turning area with almost constant speed (4 kt). When the Tx changes its direction, the Tx speed was reduced to 0.5 kt.

Let us next focus on the results obtained by the probing signals [Figs. 13(c) and 13(d)]. The figures show the relationship of the experiment time with the delay and Doppler spreads of the UWA channel, respectively. Note that the delay and Doppler spreads are corrected for the transmission loss using the Tx-Rx distance. The white dotted lines in Fig. 13(c) show the maximum delay spread that can be measured by normal D-OSDM (L) and MIMO D-OSDM ($\tilde{L}$), respectively. The white dotted lines in Fig. 13(d) show the subcarrier spacing of normal D-OSDM, MIMO D-OSDM and MIMO D-OFDM in the frequency domain, respectively.

Focusing on the delay spread of the UWA channel, Fig. 13(c) shows that we can test UWA communication with various delay spreads. The figure clearly illustrates that the delay spread of the UWA channel (-20 – 0 dB) ranges from a few to tens of milliseconds. To evaluate this more quantitatively, we calculated the RMS delay spread of the UWA channel [32]. Fig. 14 shows a histogram of the RMS delay spread using the dominant paths of the UWA channel (-20 – 0 dB). As shown in the figure, the RMS delay spread distributes from 7.5×10^{-1} (3.6 symbols) to 6.2 ms (29.7 symbols), and their average was 2.0 ms (9.6 symbols). By comparing Figs. 13(a) and 13(c), we found that the delay spread of the UWA channel becomes large when the Tx is in the starting area, and it sometimes exceeds the white dotted lines meaning that it results in interblock interference (IBI). Note that the effect of IBI on MIMO D-OSDM is larger than that on normal D-OSDM (the measurable delay spread of MIMO D-OSDM is half that of normal D-OSDM),

Furthermore, since the performance of MIMO systems depends largely on the correlation between the UWA channel coefficients, we also calculated the correlation coefficient among four significant paths between the Tx and Rx (E#0 → H#0, E#0 → H#1, E#1 → H#0 and E#1 → H#1). The correlation coefficient is computed by taking the impulse response values in each path, and then calculating the Pearson correlation coefficient between them. As a result, we found that many of the UWA channels are only slightly correlated, but some UWA channels have a high correlation value, because the spatial diversity of the Rx is weak compared to that of the Tx.

Fig. 15 shows a histogram of the channel correlation coefficient from the experiment, where a value of 0 and 1 indicates the UWA channel is low- and high-correlated, respectively. From this figure, it was found that many of the UWA channels are only slightly correlated [average correlation coefficient of (E#0 → H#0, E#1 → H#0), (E#0 → H#0, E#1 → H#1), (E#0 → H#1, E#1 → H#0) and (E#0 → H#1, E#1 → H#1) is approximately 0.3]. However, some UWA channels have a high correlation value [average correlation coefficient of (E#0 → H#0, E#0 → H#1) and (E#1 → H#0, E#1 → H#1) is 0.78 and 0.62, respectively]. This means that the spatial diversity of the Rx (H#1 and H#2) is weak compared to that of the Tx (E#1 and E#2). However, we will show that MIMO systems (MIMO D-OSDM and MIMO D-OFDM) outperform SIMO systems (normal D-OSDM) in such an environment.

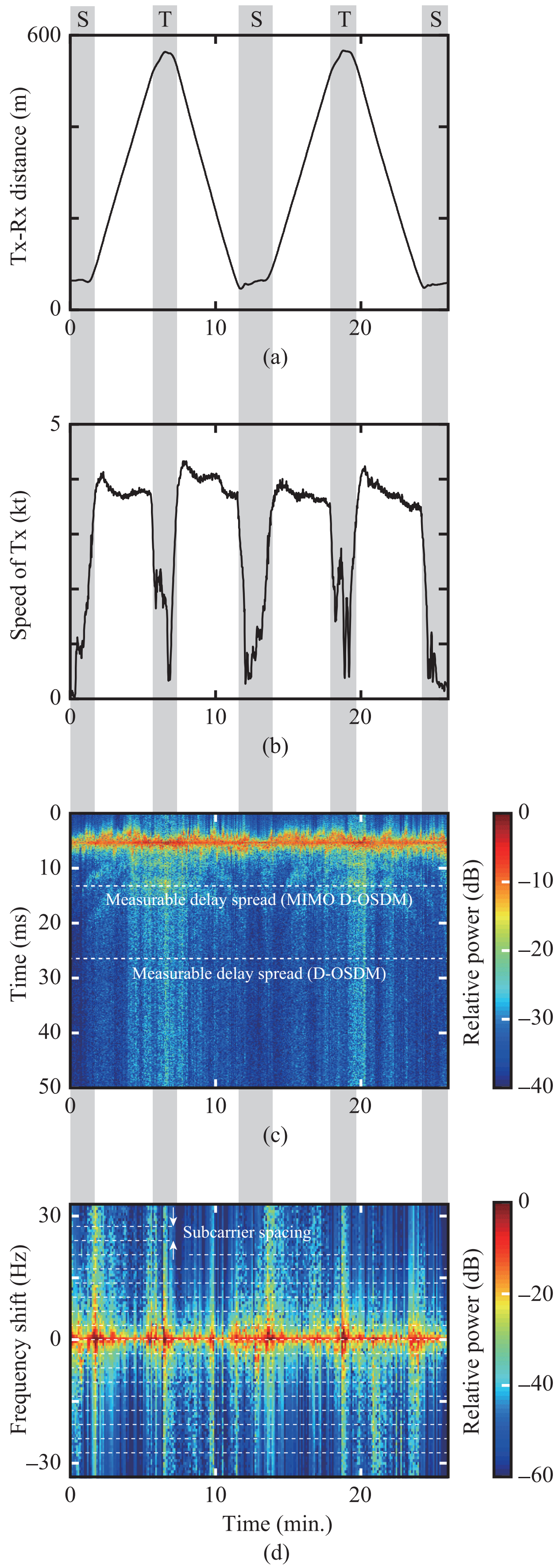

Fig. 13. Experimental environment; relationship between experiment time and (a) Tx-Rx distance, (b) speed of Tx, (c) delay spread and (d) Doppler spread of the UWA channel. 'S' and 'T' show the periods when the Tx is located at the starting area and turning area, respectively.

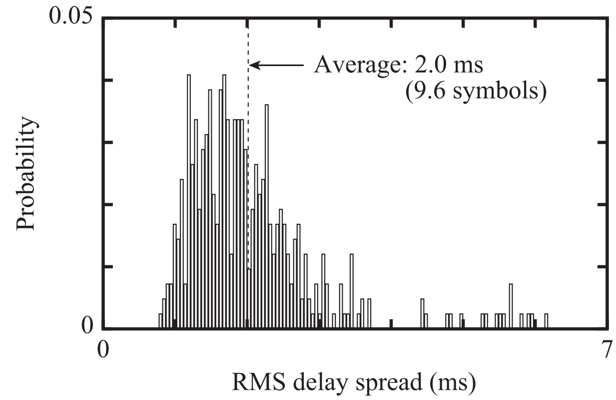

Fig. 14. Histogram of root-mean square (RMS) delay spread of the UWA channel.

Focusing on the Doppler spread of the UWA channel, it was found that the Doppler spread is large enough to boost the Doppler diversity. Note that the averaging time for the Doppler spread was 1.5 s while the block duration of the communication signal was 264.6 ms. As shown in Fig. 13(d), the maximum Doppler spread of the UWA channel (-20 – 0 dB) was about several Hertz, and sometimes spreads over 2–3 subcarrier spacings. In addition, by comparing Figs. 13(b) and 13(d), we found that the effect of the Doppler spread is dominant when the Rx is at the starting and turning area, where the velocity and direction of the Tx changes dynamically. Such an environment would be ideal for UWA communication, since the performance of MIMO D-OSDM, normal D-OSDM, and MIMO D-OFDM would be good when the normalized Doppler shift is about 2.4 times larger than the subcarrier spacing, as described in Section III.

Consequently, we can conclude that the UWA channel used in this experiment has various delay and Doppler spreads, which makes it desirable to evaluate the UWA communication performance.

C. Results of UWA communication

TABLE V
UNCODED AND CODED BLOCK ERROR RATE OBTAINED IN THE SEA TRIAL.

	Normal D-OSDM	MIMO D-OSDM	MIMO D-OFDM
Uncoded block error rate (%)	100	87.8	91.7
Coded block error rate (%)	9.7	3.2	9.3

The experimental results are shown in Figs. 16, 17, and Table V. At first, we would like to discuss whether we can compare the performance of MIMO D-OSDM, normal D-OSDM, and MIMO D-OFDM. Fig. 12 shows the Tx courses measured by GPS. As shown in the figure, the test courses of MIMO D-OSDM, normal D-OSDM, and MIMO D-OFDM are almost the same. Hence, it is considered that the performances of MIMO D-OSDM, normal D-OSDM, and MIMO D-OFDM are evaluated under almost the same experimental conditions. In the following, we show that MIMO D-OSDM can achieve more reliable UWA communication than normal D-OSDM and MIMO D-OFDM even in the experiments.

1) MIMO D-OSDM vs. normal D-OSDM: Let us compare the performance of MIMO D-OSDM and normal D-OSDM. Figs. 16(a) and 16(c) show the relationship of the experiment time with the BER (without coding) and BER (with coding), respectively. As shown in Fig. 16(a), the BER (without coding) of MIMO D-OSDM (blue points) is smaller than that of normal D-OSDM (red points) generally. This means that the advantages of MIMO D-OSDM (increase of spectrum efficiency without using a higher modulation rate) generally outweigh its disadvantages (an increase of noise due to channel approximation). On the other hand, the BER of MIMO D-OSDM is larger than that of normal D-OSDM when the Tx is in the starting area, where the delay spread of the UWA channel largely exceeds the measurable delay spread [Fig. 13(c)]. In such cases, it was found that the advantages of MIMO D-OSDM do not outweigh its disadvantages.

The advantage of MIMO D-OSDM over normal D-OSDM still holds true when we compare their performance with channel coding [Fig. 16(c)]. As shown in Fig. 16(c), the BER of MIMO D-OSDM and normal D-OSDM improves dramatically. As for the experimental results without coding, the BER of MIMO D-OSDM is smaller than that of normal D-OSDM in general, except when the Tx is in the starting area.

From the experimental results, we also found that MIMO D-OSDM has several errors even at the starting area, although normal D-OSDM achieves error-free communication [Figs. 16(a) and 16(c)]. One of the reasons considered is the existence

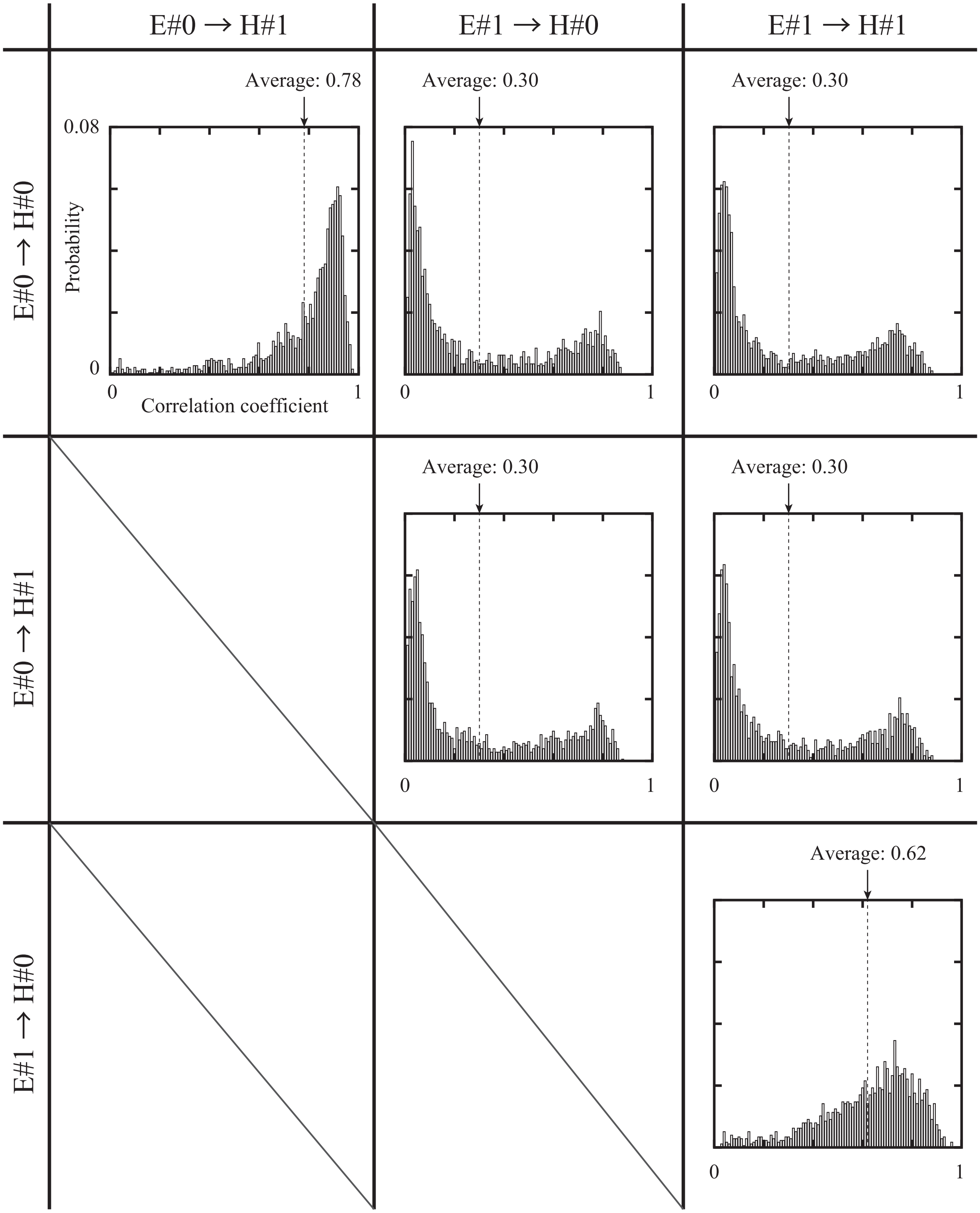

Fig. 15. Histogram of correlation coefficients of channel impulse response obtained in the experiment (E:emitter and H:hydrophone).

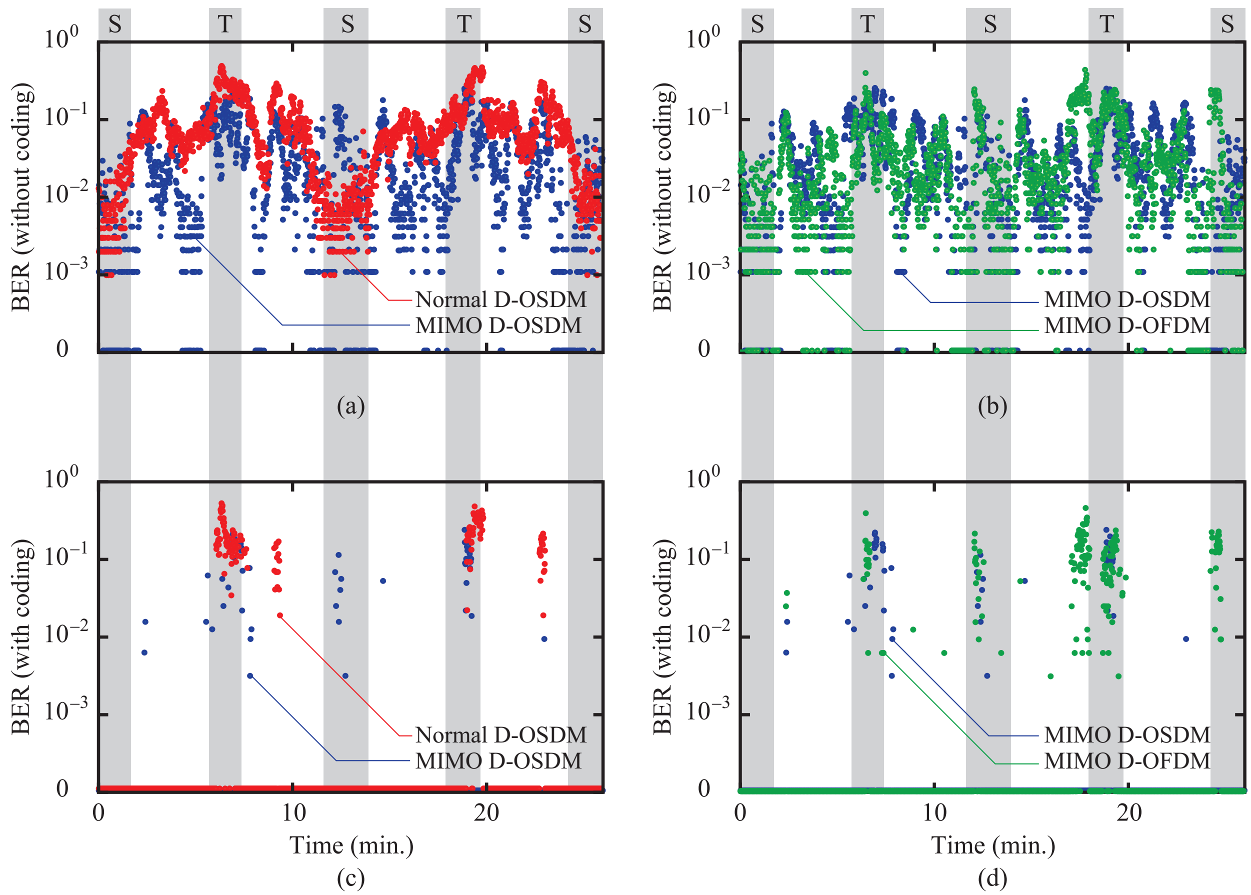

Fig. 16. Experimental results; relationship between experiment time and (a) BERs of MIMO D-OSDM and normal D-OSDM (without coding), (b) BERs of MIMO D-OSDM and MIMO D-OFDM (without coding), (c) BERs of MIMO D-OSDM and normal D-OSDM (with coding) and (d) BERs of MIMO D-OSDM and MIMO D-OFDM (with coding). 'S' and 'T' shows the periods when the Tx locates at the starting area and turning area, respectively.

of the frequency-lag among the received signals, that was considered in simulation III. As described in Section III-C, the frequency-lag among the received signals affects the performance of a MIMO system when the communication platform makes a rotational motion, and the Tx actually makes such a motion in this experiment. However, as discussed in Section III-C, such a maneuver that creates a large velocity difference between emitters or hydrophones remains rare in actual underwater vehicle operations. Hence, it would not affect communication much in actual underwater vehicle operations.

We also would like to compare the experimental results and simulation results. Figs. 17(a) and 17(c) show the relationship of the E_b/N_0 with the BER (without coding) and BER (with coding), respectively. Similar to the simulation results [Figs. 7(a) and 7(b)], it seems that MIMO D-OSDM has a better BER performance than normal D-OSDM. On the other hand, the BER of MIMO D-OSDM is sometimes larger than normal D-OSDM when the E_b/N_0 is larger than 30 dB, due to the effect of a large delay spread. These results suggest that we should use MIMO D-OSDM and normal D-OSDM depending on the delay spread length – when the delay spread greatly exceeds the guard interval, the use of normal D-OSDM would be better than the use of MIMO D-OSDM.

Finally, we would like to compare the advantage of MIMO D-OSDM over normal D-OSDM from a practical perspective. Table V shows the block error rate (BLER) of normal D-OSDM and MIMO D-OSDM. The BLER was calculated by dividing the number of erroneous blocks to the total number of transmitted blocks. As shown in the table, MIMO D-OSDM achieves a better BLER than normal D-OSDM. Especially, the BLER of MIMO D-OSDM is about 1/3 compared to that of normal D-OSDM when we use channel coding. The obtained results suggest that MIMO D-OSDM can achieve more reliable UWA communication than normal D-OSDM.

2) MIMO D-OSDM vs. MIMO D-OFDM: Let us next compare the performance of MIMO D-OSDM and MIMO D-OFDM. Figs. 16(b) and 16(d) show the relationship of the experiment time with the BER (without coding) and BER (with coding), respectively. Different from Section IV-C1, we could not observe a clear difference between the BER (without coding) of MIMO D-OSDM (blue points) and MIMO D-OFDM (green points) generally. However, the performance difference becomes clear when we focus on the communication results with channel coding [Fig. 16(d)]. As shown in Fig. 16(d), the BER of MIMO D-OSDM is smaller than that of MIMO D-OFDM in general.

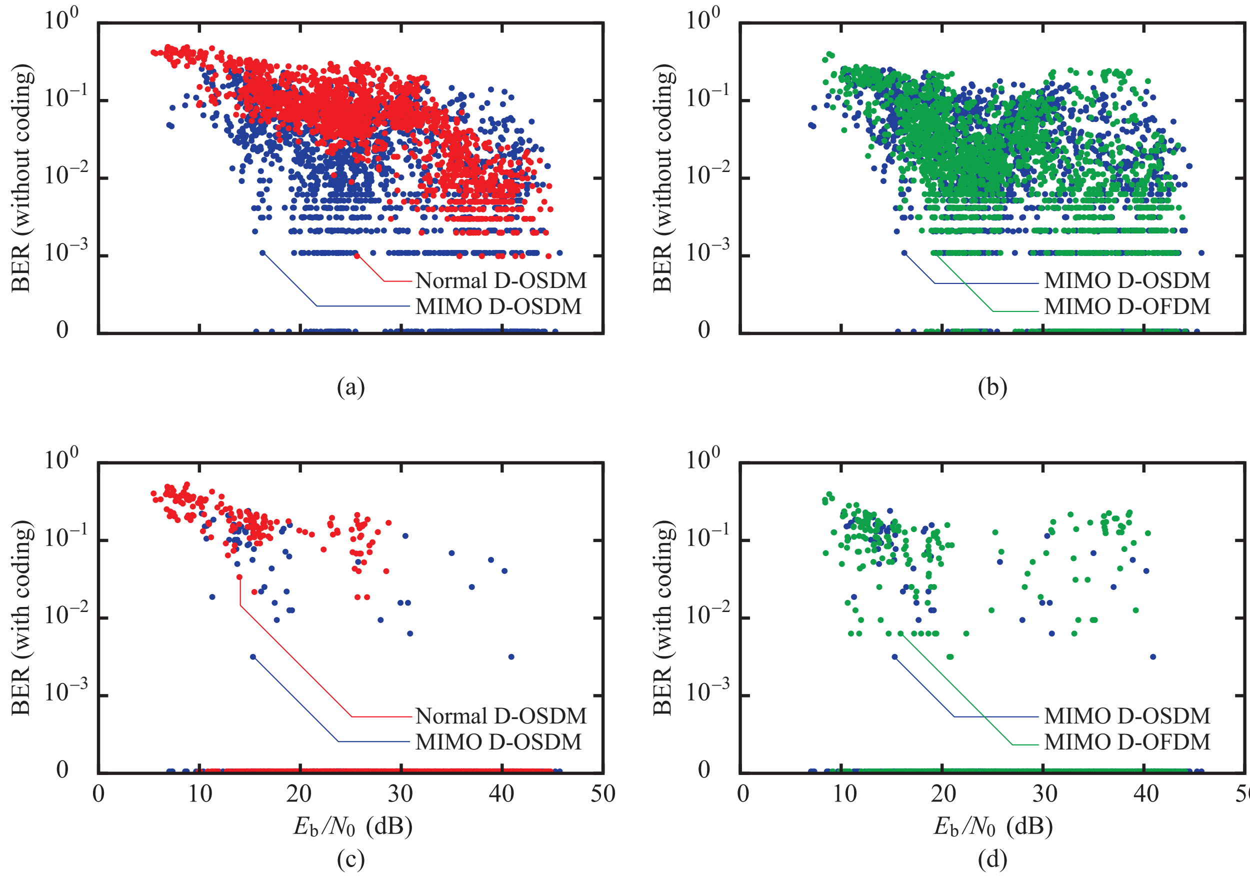

Fig. 17. Experimental results; relationship between E_b/N_0 and (a) BERs of MIMO D-OSDM and normal D-OSDM (without coding), (b) BERs of MIMO D-OSDM and MIMO D-OFDM (without coding), (c) BERs of MIMO D-OSDM and normal D-OSDM (with coding) and (d) BERs of MIMO D-OSDM and MIMO D-OFDM (with coding).

We also would like to compare the experimental results and simulation results. Figs. 17(b) and 17(d) show the relationship of the E_b/N_0 with the BER (without coding) and BER (with coding), respectively. From Fig. 17(b), we could not find a clear difference between MIMO D-OSDM and MIMO D-OFDM when we compare them without channel coding. On the other hand, the number of errors in MIMO D-OFDM seems to be larger than that of MIMO D-OSDM, when we compare them with channel coding [Fig. 17(d)].

Finally, we would like to show an advantage of MIMO D-OSDM over MIMO D-OFDM from a practical perspective. As shown in Table V, MIMO D-OSDM achieves a better BLER than normal D-OSDM. As in Section IV-C1, the BLER of MIMO D-OSDM is about 1/3 compared to that of MIMO D-OFDM when we use channel coding. The obtained results suggest that MIMO D-OSDM can also achieve more reliable UWA communication than MIMO D-OFDM.

V. Conclusion

In this paper, we have combined MIMO signaling and normal D-OSDM to achieve both energy- and spectrum-efficient UWA communication. We developed the transmitter and receiver processing for MIMO D-OSDM and showed that MIMO D-OSDM can improve the spectrum efficiency while preserving the characteristics of D-OSDM in terms of its resilience against delay and Doppler spreads. We also evaluated the performance of MIMO D-OSDM in doubly spread channels in both simulations and sea trials. The simulation and experimental results suggested that MIMO D-OSDM has an advantage over normal D-OSDM, MIMO D-OFDM and classical MIMO OFDM – MIMO D-OSDM achieved a better BER than the benchmarks. In addition, in the sea trial, the BLER of MIMO D-OSDM was about 1/3 compared to that of normal D-OSDM and MIMO D-OFDM. We can conclude that MIMO D-OSDM is a viable technique that achieves reliable and effective UWA communication. An extension of our technique to a multiuser environment and the consideration of multiuser interference is one of our future works.

Acknowledgment

The authors would like to thank Ms. S. Nishihara, Mr. H. Iwaya, Y. Umezawa, S. Endo, T. Sato, and R. Chinone (University of Tsukuba), and Mr. T. Takekoshi, K. Katsumata, and Y. Takahashi (OKI SEATEC Co., Ltd.) for their support in conducting the sea trial. This work was supported by Grant-in-Aid for Young Scientists (A) and Grant-in-Aid for Scientific Research (B), the Japan Society for the Promotion of Science (15H05560 and 19H02351).

References

[1] M. Stojanovic, "Recent advances in high-speed underwater acoustic communications," *IEEE Journal of Oceanic Engineering*, vol. 21, no. 2, pp. 125–136, Apr 1996.

[2] M. Chitre, S. Shahabudeen, and M. Stojanovic, "Underwater acoustic communications and networking: Recent advances and future challenges," *Marine Technology Society Journal*, vol. 42, pp. 103–116, 2008.

[3] Z. Zeng, S. Fu, H. Zhang, Y. Dong, and J. Cheng, "A survey of underwater optical wireless communications," *IEEE Communications Surveys Tutorials*, vol. 19, no. 1, pp. 204–238, 2017.

[4] X. Che, I. Wells, G. Dickers, P. Kear, and X. Gong, "Re-evaluation of RF electromagnetic communication in underwater sensor networks," *IEEE Communications Magazine*, vol. 48, no. 12, pp. 143–151, December 2010.

[5] R. Istepanian and M. Stojanovic, *Underwater Acoustic Digital Signal Processing and Communication Systems*. Springer US, 2013.

[6] M. Stojanovic, J. Catipovic, and J. G. Proakis, "Adaptive multichannel combining and equalization for underwater acoustic communications," *The Journal of the Acoustical Society of America*, vol. 94, no. 3, pp. 1621–1631, 1993.

[7] M. Stojanovic, J. A. Catipovic, and J. G. Proakis, "Phase-coherent digital communications for underwater acoustic channels," *IEEE Journal of Oceanic Engineering*, vol. 19, no. 1, pp. 100–111, Jan 1994.

[8] ——, "Reduced-complexity spatial and temporal processing of underwater acoustic communication signals," *The Journal of the Acoustical Society of America*, vol. 98, no. 2, pp. 961–972, 1995.

[9] M. Stojanovic, J. G. Proakis, and J. A. Catipovic, "Performance of high-rate adaptive equalization on a shallow water acoustic channel," *The Journal of the Acoustical Society of America*, vol. 100, no. 4, pp. 2213–2219, 1996.

[10] S. Coatelan and A. Glavieux, "Design and test of a coding OFDM system on the shallow water acoustic channel," in *OCEANS '95. MTS/IEEE. Challenges of Our Changing Global Environment. Conference Proceedings.*, vol. 3, Oct 1995, pp. 2065–2070 vol.3.

[11] S. F. Mason, C. R. Berger, S. Zhou, and P. Willett, "Detection, synchronization, and Doppler scale estimation with multicarrier waveforms in underwater acoustic communication," *IEEE Journal on Selected Areas in Communications*, vol. 26, no. 9, pp. 1638–1649, December 2008.

[12] B. Li, S. Zhou, M. Stojanovic, L. Freitag, and P. Willett, "Multicarrier communication over underwater acoustic channels with nonuniform Doppler shifts," *IEEE Journal of Oceanic Engineering*, vol. 33, no. 2, pp. 198–209, April 2008.

[13] Z. Wang, S. Zhou, G. B. Giannakis, C. R. Berger, and J. Huang, "Frequency-domain oversampling for zero-padded OFDM in underwater acoustic communications," *IEEE Journal of Oceanic Engineering*, vol. 37, no. 1, pp. 14–24, Jan 2012.

[14] S. J. Hwang and P. Schniter, "Efficient multicarrier communication for highly spread underwater acoustic channels," *IEEE Journal on Selected Areas in Communications*, vol. 26, no. 9, pp. 1674–1683, December 2008.

[15] G. Leus and P. A. van Walree, "Multiband OFDM for covert acoustic communications," *IEEE Journal on Selected Areas in Communications*, vol. 26, no. 9, pp. 1662–1673, December 2008.

[16] K. Tu, T. M. Duman, M. Stojanovic, and J. G. Proakis, "Multiple-resampling receiver design for OFDM over Doppler-distorted underwater acoustic channels," *IEEE Journal of Oceanic Engineering*, vol. 38, no. 2, pp. 333–346, April 2013.

[17] Y. M. Aval and M. Stojanovic, "Differentially coherent multichannel detection of acoustic OFDM signals," *IEEE Journal of Oceanic Engineering*, vol. 40, no. 2, pp. 251–268, April 2015.

[18] B. Li, J. Huang, S. Zhou, K. Ball, M. Stojanovic, L. Freitag, and P. Willett, "MIMO-OFDM for high-rate underwater acoustic communications," *IEEE Journal of Oceanic Engineering*, vol. 34, no. 4, pp. 634–644, Oct 2009.

[19] P. C. Carrascosa and M. Stojanovic, "Adaptive channel estimation and data detection for underwater acoustic MIMO-OFDM systems," *IEEE Journal of Oceanic Engineering*, vol. 35, no. 3, pp. 635–646, July 2010.

[20] K. Pelekanakis and A. B. Baggeroer, "Exploiting space-time-frequency diversity with MIMO-OFDM for underwater acoustic communications," *IEEE Journal of Oceanic Engineering*, vol. 36, no. 4, pp. 502–513, Oct 2011.

[21] J. Huang, S. Zhou, and Z. Wang, "Performance results of two iterative receivers for distributed MIMO OFDM with large Doppler deviations," *IEEE Journal of Oceanic Engineering*, vol. 38, no. 2, pp. 347–357, April 2013.

[22] J. Han, L. Zhang, and G. Leus, "Partial FFT demodulation for MIMO-OFDM over time-varying underwater acoustic channels," *IEEE Signal Processing Letters*, vol. 23, no. 2, pp. 282–286, Feb 2016.

[23] T. Ebihara and G. Leus, "Underwater acoustic communication using Doppler-resilient orthogonal signal division multiplexing," in *OCEANS 2014 - TAIPEI*, April 2014, pp. 1–4.

[24] ——, "Doppler-resilient orthogonal signal-division multiplexing for underwater acoustic communication," *IEEE Journal of Oceanic Engineering*, vol. 41, no. 2, pp. 408–427, Apr. 2016.

[25] T. Ebihara and K. Mizutani, "Underwater acoustic communication with an orthogonal signal division multiplexing scheme in doubly spread channels," *IEEE Journal of Oceanic Engineering*, vol. 39, no. 1, pp. 47–58, Jan. 2014.

[26] G. Leus, S. Zhou, and G. B. Giannakis, "Orthogonal multiple access over time- and frequency-selective channels," *IEEE Transactions on Information Theory*, vol. 49, no. 8, pp. 1942–1950, Aug 2003.

[27] T. Ebihara, G. Leus, and H. Ogasawara, "Underwater acoustic communication using Doppler-resilient orthogonal signal division multiplexing in a harbor environment," *Physical Communication*, vol. 27, pp. 24–35, 2018.

[28] J. Han, W. Shi, and G. Leus, "Space-frequency coded orthogonal signal-division multiplexing over underwater acoustic channels," *The Journal of the Acoustical Society of America*, vol. 141, no. 6, pp. EL513–EL518, 2017.

[29] J. Han and G. Leus, "Space-time and space-frequency block coded vector OFDM modulation," *IEEE Communications Letters*, vol. 21, no. 1, pp. 204–207, Jan 2017.

[30] F. Qu and L. Yang, "Basis expansion model for underwater acoustic channels?" in *OCEANS 2008*, Sept 2008, pp. 1–7.

[31] K. F. Scussel, J. A. Rice, and S. Merriam, "A new MFSK acoustic modem for operation in adverse underwater channels," in *Oceans '97. MTS/IEEE Conference Proceedings*, vol. 1, Oct 1997, pp. 247–254 vol.1.

[32] A. Goldsmith, *Wireless Communications*. Cambridge University Press, 2005, ch. 3.3, p. 87.

[33] A. M. Sayeed and B. Aazhang, "Joint multipath-Doppler diversity in mobile wireless communications," *IEEE Transactions on Communications*, vol. 47, no. 1, pp. 123–132, Jan 1999.

[34] Y. H. Eng, K. M. Teo, M. Chitre, and K. M. Ng, "Online system identification of an autonomous underwater vehicle via in-field experiments," *IEEE Journal of Oceanic Engineering*, vol. 41, no. 1, pp. 5–17, Jan 2016.

PLACE
PHOTO
HERE

Tadashi Ebihara Tadashi Ebihara was born in Tokyo, Japan, in 1986. He received the Ph.D. degree from the University of Tsukuba, Tsukuba, Japan, in 2010. He received the Research Fellowship for Young Scientists (DC1), Japan Society for the Promotion of Science (JSPS), 2009-2010. From September 2013 till December 2013 he was a Visiting Professor at the Delft University of Technology, The Netherlands. He is currently an Associate Professor at the Faculty of Engineering, Information and Systems, University of Tsukuba. His research interests include mobile communications and their applications to underwater acoustic communication systems. Tadashi Ebihara received a 2017 IEEE Oceanic Engineering Society Japan Chapter Young Researcher Award.

PLACE
PHOTO
HERE

Hanako Ogasawara Hanako Ogasawara was born in Kochi, Japan. She received the Ph.D. degree from the University of Tsukuba, Tsukuba, Japan, in 2009. She worked as a post-doctoral researcher at Scripps Institution of Oceanography, UC San Diego, 2011-2012. She is currently as an Associate Professor at National Defense Academy of Japan. Her research topic is underwater acoustic monitoring including ocean acoustic tomography.

PLACE
PHOTO
HERE

Geert Leus Geert Leus was born in Leuven, Belgium, in 1973. He received the electrical engineering degree and the PhD degree in applied sciences from the Katholieke Universiteit Leuven, Belgium, in June 1996 and May 2000, respectively. He has been a Research Assistant and a Postdoctoral Fellow of the Fund for Scientific Research - Flanders, Belgium, from October 1996 till September 2003. During that period, Geert Leus was affiliated with the Electrical Engineering Department of the Katholieke Universiteit Leuven, Belgium. Currently, Geert Leus is a Professor at the Faculty of Electrical Engineering, Mathematics and Computer Science of the Delft University of Technology, The Netherlands. During the summer of 1998, he visited Stanford University, and from March 2001 till May 2002 he was a Visiting Researcher and Lecturer at the University of Minnesota. His research interests are in the area of signal processing for communications. Geert Leus received a 2002 IEEE Signal Processing Society Young Author Best Paper Award and a 2005 IEEE Signal Processing Society Best Paper Award.